Mechanical Properties in Metal-Organic Frameworks: Emerging Opportunities and Challenges for Device Functionality and Technological Applications

Burtch, N.C.; Heinen, J.; Bennett, T.D.; Dubbeldam, D.; Allendorf, M.D.

DOI
10.1002/adma.201704124

Publication date
2018

Document Version
Final published version

Published in
Advanced materials

ADVANCED MATERIALS
www.advmat.de

Mechanical Properties in Metal–Organic Frameworks: Emerging Opportunities and Challenges for Device Functionality and Technological Applications

Nicholas C. Burtch, Jurn Heinen, Thomas D. Bennett, David Dubbeldam, and Mark D. Allendorf**

Some of the most remarkable recent developments in metal–organic framework (MOF) performance properties can only be rationalized by the mechanical properties endowed by their hybrid inorganic–organic nanoporous structures. While these characteristics create intriguing application prospects, the same attributes also present challenges that will need to be overcome to enable the integration of MOFs with technologies where these promising traits can be exploited. In this review, emerging opportunities and challenges are identified for MOF-enabled device functionality and technological applications that arise from their fascinating mechanical properties. This is discussed not only in the context of their more well-studied gas storage and separation applications, but also for instances where MOFs serve as components of functional nanodevices. Recent advances in understanding MOF mechanical structure–property relationships due to attributes such as defects and interpenetration are highlighted, and open questions related to state-of-the-art computational approaches for quantifying their mechanical properties are critically discussed.

1. Introduction

Metal–organic frameworks (MOFs), also known as porous coordination polymers, are an emerging class of nanoporous materials constructed from metal-based nodes bridged by coordination bonds to multidentate ligands (**Figure 1**a).[1–4] An explosion of interest in these hybrid materials has resulted from their unprecedented degree of structural and functional tunability, due to the elements of rational design enabled by their wide array of possible organic and inorganic building blocks with known geometries and coordination states.[5] Beyond their extraordinarily high porosity characteristics,[6,7] the rich synthetic chemistry of MOFs also enables the incorporation of highly desirable properties such as coordinatively unsaturated metal sites[8] and amine-functionalized groups[9,10] that are inaccessible to purely inorganic zeolites.

Within a field which has already generated tens of thousands of highly ordered crystalline porous structures,[11] a survey of the recent patent literature also indicates that MOF research has progressed to the point where their structural characteristics can be exploited for an array of promising technological applications.[12] The time-to-market from creation to commercial application for new materials generally averages around twenty years;[13] in line with this timeframe, the accumulation of MOF research has recently reached a turning point with the launch of the first commercial MOF products for the storage and delivery of toxic gases such as arsine and phosphine.[14] While explored in greatest depth for their remarkable gas separation and storage capabilities,[15] experts in fields ranging from materials science and physics to electrical engineering are also now being engaged to overcome the fundamental challenges needed to propel MOFs toward a broader array of applications that include electronic devices and chemical sensors (Figure 1b).[16,17]

Due to their hybrid inorganic–organic nature, MOFs possess attractive characteristics that are absent from purely inorganic or organic systems. MOFs can exhibit, for example, higher thermal stabilities than organic polymers[18] while maintaining a degree of mechanical flexibility that is largely inaccessible to inorganic materials. By conventional mechanical property metrics such as the Young's modulus and hardness, MOFs also bridge a design space that spans those of both traditional "soft" and "hard" materials.[19] However, it is this hybrid nature combined with their permanent porosity that leads to some of their most attractive characteristics from an applications standpoint. For example, dynamic behaviors under applied stress are observed that make these "soft-porous"[20] network structures flexible[21] or stimuli-responsive.[22,23] Although many phenomena fall within the realm of flexible materials, such as gate-opening,[24,25] breathing,[26] and structural rotation,[27] all involve

Dr. N. C. Burtch, Dr. M. D. Allendorf
Sandia National Laboratories
Livermore, CA 94551, USA
E-mail: nburtch@sandia.gov; mdallen@sandia.gov
J. Heinen, Dr. D. Dubbeldam
Van't Hoff Institute for Molecular Sciences
University of Amsterdam
Science Park 904, 1098 XH Amsterdam, The Netherlands
Dr. T. D. Bennett
Department of Materials Science and Metallurgy
University of Cambridge
27 Charles Babbage Road, Cambridge CB3 0FS, UK
The ORCID identification number(s) for the author(s) of this article can be found under https://doi.org/10.1002/adma.201704124.

DOI: 10.1002/adma.201704124

some degree of structural change, which will lead not only to a variation in porosity but also in mechanical properties.[28] These stimuli-responsive effects also explain the relatively high prevalence of anomalous structural behaviors that are rare or unprecedented in other materials, including negative gas adsorption[29] and negative thermal expansion.[30]

While these mechanical properties are at the heart of some of the most fascinating recent findings in the MOF literature, they can also present challenges for their integration with technological applications. The purpose of this review is to provide our perspective on some of the most pressing challenges and opportunities for devices and technological applications that arise from the unusual mechanical properties of MOFs. We will also highlight open questions in the emerging field of porous materials science related to state-of-the-art computational approaches for quantifying MOF mechanical properties and present advances in understanding the effects of defects[31] and interpenetration[32] on mechanical structure-property relationships.

2. Quantifying Mechanical Properties

The concepts of stress and strain are fundamental to understanding mechanical properties in solids. While strain describes the degree of deformation that a material undergoes, stress describes its restoring force per unit area. Mechanical properties in solids can thus be characterized by their stress–strain behavior, with elastic materials exhibiting a reversible response to strain whereas plastically deformed materials undergo irreversible changes. Viscoelasticity describes a third category of behavior whereby a time-dependent and dampened elastic response to strain is exhibited; although this has been well-studied in materials such as polymers,[34] it has primarily been studied in the MOF literature in the context of gel-derived MOFs.[35]

Within the elastic regime, a complete description of a material's response to stress is provided by its elastic constant tensor. From this tensor, elastic properties such as the bulk modulus B, Young's (elastic) modulus E, Poisson's ratio ν, and shear modulus G (**Figure 2**) can be calculated, for instance using the Voigt–Reuss–Hill approximation.[36,37] The elastic constant tensor can also provide fundamental insight that is useful for understanding additional mechanical and thermal properties; in inorganic materials, for example, the elastic constant tensor correlates with mechanical properties such as ductility and hardness[38,39] and thermal properties such as heat capacity, thermal conductivity, and coefficient of thermal expansion.[40–43] Combined with finite element analysis, the elastic constant tensor can also be used to predict the elastic response of composite materials.[44] While we are aware of only one report of the elastic constant tensor being experimentally measured in a MOF,[45] a greater number of computational studies have reported this property, as discussed in section 2.2.

The purpose of the following sections is to summarize the state-of-the-art in experimental and computational approaches for quantifying MOF mechanical properties. Considering the discussion of relevant experimental techniques in the review of Tan and Cheetham,[19] we will only briefly revisit this topic here, with an emphasis on experimental techniques that have only been demonstrated since their review was published. Computationally, a comprehensive review discussing the theoretical framework for calculating MOF elastic constant tensors using atomistic simulations has not yet been presented. We will therefore critically review this topic in greater detail, including open questions of ongoing debate related to calculating the elastic constant tensors of crystalline materials under stress.

Nicholas C. Burtch is a Harry S. Truman Fellow at Sandia National Laboratories in Livermore, California. He received his B.S.E. from the University of Michigan and Ph.D. from the Georgia Institute of Technology, both in chemical engineering. His research interests include the design and synthesis of nanoporous metal–organic frameworks for materials science and adsorption applications that include multifunctional composite materials and selective gas separations.

Mark D. Allendorf is Director of the Hydrogen Advanced Materials Research Consortium (HyMARC) and a Senior Scientist at Sandia National Laboratories in Livermore, California. He holds degrees in chemistry from Washington University in St. Louis (A.B.) and received his Ph.D. in inorganic chemistry at Stanford. At Sandia, his research focuses on the fundamental science and applications of metal–organic frameworks (MOFs) and hydrogen storage. Current interests include chemical sensing, gas separations, MOFs for electronic devices, and catalysts for biofuels production. He is President Emeritus and Fellow of The Electrochemical Society.

2.1. Experimental Measurements

Well-established techniques for experimentally measuring MOF mechanical properties over the past decade have included high pressure crystallography, nanoindentation, and atomic force microscopy (AFM).[19] These techniques can be used to determine material properties such as the bulk modulus, hardness, and Young's modulus. High-pressure crystallography can be performed on single crystal or polycrystalline specimens, by enclosing the sample within a diamond anvil cell, to provide hydrostatic sample compression.[46] From these measurements, the change in crystallographic volume as a function of pressure

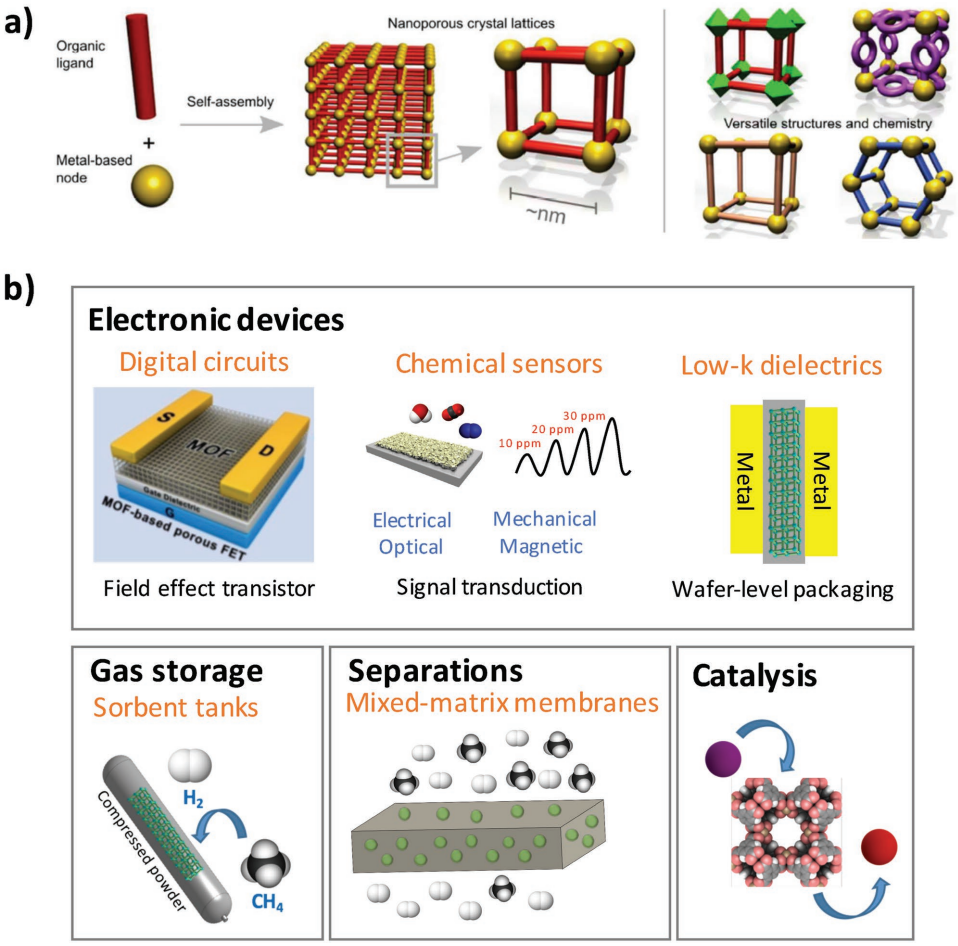

Figure 1. a) Diverse MOF structural chemistry enabled by tunable ligand, metal, and topology characteristics. Adapted with permission.[17] Copyright 2017, The Royal Society of Chemistry. b) Selected MOF-enabled device and application categories. Adapted with permission.[33] Copyright 2016, American Chemical Society.

can be analyzed and the bulk modulus obtained. Nanoindentation and AFM are related techniques in which the application of a tip is used to probe local mechanical properties. Whereas an AFM tip laterally scans a material surface to probe properties such as the roughness and Young's modulus, nanoindentation can be applied to determine the Young's modulus and hardness at a single point, down even to the nanometer scale, via the applied load versus penetration curve. As noted elsewhere,[19] care should be taken in extracting Young's modulus values from nanoindentation experiments, given the potentially anisotropic material response and nonunidirectional stress fields created by the indenter tip, which violate the assumptions of the Oliver and Pharr method for analyzing modulus data. Furthermore, careful calibration and consideration of tip shape and radius of curvature effects should be made prior to the analysis.[47,48] Nanoindentation generally gives Young's modulus values within about 50% of the calculated value, which can be due to a number of factors that include defects and anisotropy. Bulk properties, such as the bulk modulus, tend to give much better agreement.[49] Another discrepancy to consider is that theoretical properties calculated using density functional theory (DFT) are at 0 K, whereas experiments are always at finite temperatures. To enable more quantitative comparisons, it is vital that the temperature-dependency of MOF mechanical properties be better understood. This requires that more accurate molecular models and efficient simulation methodologies should be developed, as discussed in section 2.2.3.

Since the review of Tan and Cheetham,[19] additional mechanical property characterization techniques beyond those mentioned above have been applied to MOFs. In 2012, Brillouin spectroscopy was first used to elucidate the elasticity properties of the MOF ZIF-8 [$Zn(mIm)_2$] where mIm = 2-methylimidazolate.[45] Via Brillouin scattering and subsequent solution of Christoffel's matrix,[50] this powerful analysis enables a complete description of the elasticity of a material by determining its full set elastic constants. These elastic constants can also can be directly compared to the computationally calculated values and, in the case of ZIF-8, was used to understand the exceptionally low shear modulus (G_{min} of <1 GPa)[45] that underlies its irreversible pressure-induced amorphization behavior.[51]

Understanding of MOF mechanical properties would be accelerated by the development of more facile experimental

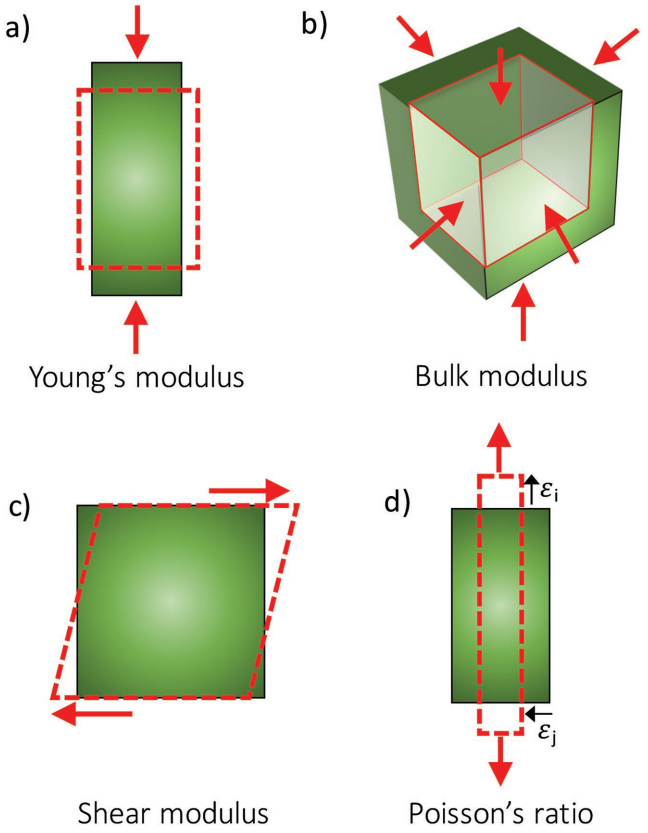

Figure 2. Depictions of selected elasticity properties in solids: a) Young's (elastic) modulus E as a measure of stiffness under unidirectional loading, b) bulk modulus B as a measure of volumetric stiffness under static pressure, c) shear modulus G as a measure of the stiffness when subjected to opposing shear forces, and d) Poisson's ratio ν as the ratio of lateral strain (ε_j) to axial strain (ε_i) upon axial loading.

techniques to extract the wealth of information available from a material's elastic constants. Brillouin spectroscopy measurements require large MOF single crystals that preclude the study of polycrystalline morphologies. Recently, a novel technique was presented, in which surface acoustic wave velocities induced by a femtosecond laser are measured using polished surfaces of polycrystalline samples under a polydimethylsiloxane film grating.[52] This approach was demonstrated through the accurate measurement of the elastic constants in seven polycrystalline metal samples and yielded agreement within 6.8% of the single crystal measurement values. The application of this technique to MOFs would be an important development and could potentially lead to a database of experimental elastic constants needed to validate the accuracy of the increasing number of computed elastic constants being obtained from DFT calculations. For the measurement of elastic moduli, bimodal amplitude modulated-frequency modulated AFM was recently applied to a series of microcrystalline MOF nanoparticles (100–500 nm), avoiding the need for the relatively large single crystals often used for extracting this information from nanoindentation experiments.[53]

If one wants to understand the intrinsic mechanical properties of a MOF, care should be taken to ensure that residual solvent is first removed from the pore space, often via solvent exchange, heat and/or vacuum treatment. The presence of guest molecules can have an appreciable effect on the measured mechanical properties. While a modest (reversible) increase in the Young's modulus of ZIF-8 from ≈2.97 to ≈3.20 GPa is observed from nanoindentation experiments on its {110} facet when going from an evacuated to DMF-solvated state,[54] more significant changes were observed in single crystals of the flexible structure $Zn_2(L)_2(DABCO)$ (L = linear dicarboxylate linker, DABCO = 1,4-diazabicyclo[2.2.2]octane) when exposed to various solvents (e.g., from ≈2.08 GPa with *N*,*N*-dimethylformamide (DMF) to ≈6.53 GPa with toluene on the {001} facet of $Zn_2(NO_2\text{-}BDC)_2(DABCO)$ where BDC = 1,4-benzenedicarboxylate), attributed to guest-induced changes to the network geometry.[55] Related considerations due to sample porosity also must be taken into account when interpreting bulk modulus values from high pressure crystallography experiments. In such experiments, a pressure-transmitting fluid is often used within the diamond anvil cell to allow hydrostatic compression of the material. Depending on the size and flexibility of the MOF pores relative to that of the pressure-transmitting media, there can be media penetration that has a significant impact on the bulk modulus.[56] A recent review summarizes these effects[57] and finds that guest molecule incorporation tends to increase the bulk modulus of MOFs. Similar effects due to guest inclusion have also been reported in high pressure crystallography studies conducted on zeolites.[58]

As interest in MOF-enabled electronic devices has grown,[17] studies of the mechanical properties of MOF thin films have emerged. Beyond the aforementioned bulk modulus, Young's modulus, and hardness properties, mechanical characteristics such as film adhesion and bending resilience on a substrate become important. Nanoscratching is a mode of operation that can be implemented in many nanoindentation instruments by laterally translating the indenter tip at set loads to provide information about the adhesion strength, abrasion, and wear resistance of a film. The first nanoscratching study was reported in 2013 on dense, electrochemically grown MOF films on Cu-electrodes.[59] Bending tests whereby the tensile strength during exposure to strain at different bending radii is an important test for flexible electronic devices,[60] and such testing has also been investigated in two recent MOF studies.[61,62] Further context on the findings of these device-related mechanical characterization studies and their implications for electronic devices is discussed in section 4.2.

2.2. Theoretical Calculations

Molecular modeling has made significant strides in the past decade toward understanding MOF structural and performance properties, ranging from the prediction of performance characteristics for structures that have yet to be synthesized to providing insight into nanoscale mechanisms that are difficult to observe experimentally.[63] While the majority of past work has focused on understanding MOF adsorption and diffusion properties, a growing number of recent efforts have focused on mechanical property modeling[64] to better understand the origins of their stimuli-responsive behavior. Given the relative

infancy of this research area, we believe that a critical review of the theoretical foundations behind the state-of-the-art approaches being used in literature is merited to ensure that open questions related to their applicability are recognized by the greater MOF community.

Although our theoretical understanding of MOF mechanical properties is largely confined to their elasticity, initial insights into possible mechanisms of plastic deformation have also recently been reported.[65] The quantitative modeling of such behavior and its comparison to experiment, however, is more challenging as plastic deformation describes a nonequilibrium phenomenon that involves residual defects that are also dependent upon the time over which the load is applied. The level of understanding needed to critically review this topic in the context of MOFs is not yet present and is thus outside the scope of this review. However, to stimulate further work in this important area, we refer the reader to literature where computational methodologies used to understand plastic deformation in other material classes are discussed.[66–68]

In this section, we critically discuss the fundamentals of how molecular modeling can be used to obtain information related to a crystalline material's elasticity. We start with a brief introduction to the ways that atomic-scale stress–strain relationships are defined, as well as the basic theory of mechanical properties in crystals. We then proceed to introduce the common approaches by which the elastic constant tensor can be calculated in crystalline solids using classical (force field) and *ab initio* (density functional theory) modeling approaches.

2.2.1. Stress–Strain Conventions and Their Connection to Continuum Properties

There are two common conventions that are used to describe the strain on a material: the Lagrangian and Eulerian formulations. In both cases, the second-order strain tensor must be defined to describe the deformation from some reference state to the actual configuration in a strained crystal. To arrive at this strain tensor, we first assign a displacement vector u to every point in the object, such that the current coordinates (r_x, r_y, r_z) are expressed in term of their reference coordinates $(\tilde{r}_x, \tilde{r}_y, \tilde{r}_z)$ as $r = r(\tilde{r})$. The two definitions of the strain (or deformation) vector u in their Lagrangian or Eulerian formulations, respectively, are given as

$$u(\tilde{r}) = r(\tilde{r}) - \tilde{r} \tag{1}$$

$$u(r) = r - \tilde{r}(r) \tag{2}$$

The configuration (or deformation) gradient F can then be defined as a second-order tensor whose components are partial derivatives of the components of r with respect to the reference configuration coordinates

$$F = F_{\alpha\beta} = \frac{\partial r_\alpha}{\partial \tilde{r}_\beta} \tag{3}$$

From the above strain vector definitions, we arrive at the two main forms of the strain tensor. The first form, the Lagrangian (Green) strain η, describes the strain in terms of material coordinates[69]

$$\eta = \eta_{\alpha\beta} = \frac{1}{2}\left(\frac{\partial u_\alpha}{\partial \tilde{r}_\beta} + \frac{\partial u_\beta}{\partial \tilde{r}_\alpha} + \frac{\partial u_\gamma}{\partial \tilde{r}_\alpha}\frac{\partial u_\gamma}{\partial \tilde{r}_\beta}\right) = \frac{1}{2}\left(F\,F^T - 1\right) \tag{4}$$

where as the second form, the Eulerian (Alsmansi) strain ϵ, uses spatial coordinates fixed in space

$$\boldsymbol{\epsilon} = \boldsymbol{\epsilon}_{\alpha\beta} = \frac{1}{2}\left(\frac{\partial u_\alpha}{\partial r_\beta} + \frac{\partial u_\beta}{\partial r_\alpha} - \frac{\partial u_\gamma}{\partial r_\alpha}\frac{\partial u_\gamma}{\partial r_\beta}\right) = \frac{1}{2}\left(1 - F^{-T}F^{-1}\right) \tag{5}$$

where 1 denotes the unit tensor and the Einstein summation convention is used. If the two gradients that are multiplied together in the third term of the above equation are small compared to unity then their product can be neglected, leading to a simplified equation termed the infinitesimal Cauchy strain tensor $\varepsilon_{\alpha\beta}$

$$\varepsilon = \varepsilon_{\alpha\beta} = \frac{1}{2}\left(\frac{\partial u_\alpha}{\partial r_\beta} + \frac{\partial u_\beta}{\partial r_\alpha}\right) \tag{6}$$

This symmetric second-order tensor is convenient and widely used because it is a measure of the linear strain and is therefore additive, decoupling translation from rotation.

Stress is a macroscopic concept that was introduced into the theory of elasticity by Cauchy as a measure of the average amount of force exerted per unit area. The Cauchy stress tensor, which is compatible with the Eulerian equations of motion, is the most commonly used measure of stress. Also referred to as the "true stress" in the engineering fields, the Cauchy stress tensor is a nine-component second-order tensor with six asymmetric components that relates the forces in the deformed configuration to areas in the present configuration. There also exists the first Piola-Kirchhoff stress tensor that describes forces in the deformed configurations in terms of the surface area in the reference configuration and the second Piola-Kirchhoff stress tensor that relates forces in the reference configuration to areas in the reference configuration.[70] Whereas the first nonsymmetric Piola-Kirchhoff stress tensor is used in the Lagrangian equations of motion, the second Piola-Kirchhoff stress tensor is symmetric and is therefore more suitable than the first Piola-Kirchhoff stress tensor for use in stress–strain relations.

The work of Irving and Kirkwood provides the link between microscopic properties and macroscopic density, momentum, and energy at a fixed Eulerian point by utilizing an important property of the Dirac delta function

$$h(\boldsymbol{r}) = \int_{-\infty}^{\infty} \delta(\boldsymbol{r}_i - \boldsymbol{r})\, h(\boldsymbol{r}_i)\, d\boldsymbol{r}_i \tag{7}$$

where r is the location in space of the Eulerian reference and r_i is the location of molecule i. The equations of motion in the Eulerian frame are given by expressing the flow through this infinitesimal control volume in the continuum or by application of the Dirac delta function in the discrete system. The time derivatives of state properties can be used to obtain the fluxes and to obtain the Irving-Kirkwood (IK) stress tensor[71,72]

$$\Pi = \sum_{i=1}^{N} \left\langle m_i \left(\frac{\boldsymbol{p}_i}{m_i} - \boldsymbol{u} \right) \left(\frac{\boldsymbol{p}_i}{m_i} - \boldsymbol{u} \right) \delta(\boldsymbol{r}_i - \boldsymbol{r}) + \frac{1}{2} \sum_{j \neq i}^{N} \boldsymbol{f}_{ij} \; \boldsymbol{r}_{ij} O_{ij} \delta(\boldsymbol{r}_i - \boldsymbol{r}) \right\rangle \quad (8)$$

where u is the streaming velocity, p is the momentum, and the so-called IK operator is

$$O_{ij} = \left(1 - \frac{1}{2} r_{ij} \cdot \frac{\partial}{\partial \boldsymbol{r}_i} + \cdots + \frac{1}{n!} \left(- r_{ij} \cdot \frac{\partial}{\partial \boldsymbol{r}_i} \right)^{n-1} + \cdots \right) \quad (9)$$

The virial pressure is obtained from Equation (8) in a closed volume V and by taking only the first term in the IK operator of Equation (9), known as the IK1 approximation, so that $\delta(\mathbf{r}_i - \mathbf{r}) = 1$ and $Oij\ \delta(\mathbf{r}_i - \mathbf{r}) = 1$. The virial form of pressure is the most widely used version in the molecular dynamics literature due to its simplicity. However, the virial form can only be used to provide a single pressure tensor for an entire isolated system. For nonequilibrium systems, a localized description such as the IK stress must be used. For more details on the connection between the continuum formulation and the molecular system, the reader is referred to several reviews on the topic.[72–75]

The Cauchy stress σ, first Piola-Kirchoff stress P, and second Piola-Kirchhoff stress t are related through the configuration gradient F[70,76]

$$P = |F| \, \sigma F^{-T} \quad (10)$$

$$t = |F| \, F^{-1} \sigma F^{-T} \quad (11)$$

$$t = F^{-1} \, P \quad (12)$$

Molecular dynamics simulations can be analyzed in a Eulerian or a Lagrangian reference frame, and there is some exploratory work that measures the differences between the Cauchy stress, the virial equation, and first Piola-Kirchhoff stress converted to Cauchy stress.[77] The difference between these three quantities is negligible for constrained volumes, and for larger deformations of 1–5% at 300–600 K the difference between the hydrostatic virial stress and the hydrostatic transformed Piola-Kirchhoff stress is still very small with a difference of 1% at most. For the above comparisons, the reference material configuration was chosen to be the zero temperature, undeformed state of the system.

2.2.2. Mechanical Properties in Crystals

The elasticity tensor $C_{\alpha\beta\mu\nu}$ is described in the Einstein summation notation by Hooke's law as[78]

$$\sigma_{\alpha\beta} = C_{\alpha\beta\mu\nu} \, \varepsilon_{\mu\nu} \quad (13)$$

which relates the stress σ to the strain ε via a 6×6 elastic tensor. A systematic study of lattice stability was done by Born and Huang[79] who formulated their stability criteria in terms of the elastic constants by expanding the internal crystal energy in a power series in the strain and imposing convexity of the energy. This criteria expresses the fact that any mechanical strain must increase the total mechanical energy of a system at equilibrium, resulting from the requirement that the eigenvalues of the elastic constants matrix C be positively defined. The eigenvectors are the deformation modes, and the convexity of the internal energy function is not coordinate invariant.[80] Importantly, one implication that arises from the convexity of the internal energy function not being coordinate invariant is that, under applied load, different definitions of strain lead to different Born stability conditions.

Born and Huang[79] and Wallace[81] also outlined the basic theory to calculate the thermodynamic properties of perfect crystals from their interatomic potential functions. The correct formulation of the thermodynamics of strained crystals was derived by Wallace, where the elastic constants can be defined from one of three approaches:

(1) Second derivative of the internal energy and Helmholtz free energy with respect to deformation parameters u, infinitesimal strains ε, the Eulerian tensor ε, or Lagrangian strain tensor η.
(2) First derivative of Cauchy or thermodynamic stress with respect to the various strains, or
(3) equations of motions (i.e., sound velocities).

For example, using approach (1), the elastic constants can be defined at an arbitrary configuration $\tilde{r}$, where the strains $\eta_{\alpha\beta}$ are measured from $\tilde{r}$ and the derivatives are evaluated at $\tilde{r}$ (i.e., at $\eta_{\alpha\beta} = 0$). The internal energy U and Helmholtz free energy A may then be expanded in powers of the strains $\eta_{\alpha\beta}$

$$U(\tilde{r}, S, \eta_{\alpha\beta}) = U(\tilde{r}, S) + V \sum_{\alpha\beta} t_{\alpha\beta} \eta_{\alpha\beta} + \frac{1}{2} V \sum_{\alpha\beta\gamma\delta} C^{S}_{\alpha\beta\gamma\delta} \eta_{\alpha\beta} \eta_{\gamma\delta} + \ldots \quad (14)$$

$$A(\tilde{r}, T, \eta_{\alpha\beta}) = A(\tilde{r}, T) + V \sum_{\alpha\beta} t_{\alpha\beta} \eta_{\alpha\beta} + \frac{1}{2} V \sum_{\alpha\beta\gamma\delta} C^{T}_{\alpha\beta\gamma\delta} \eta_{\alpha\beta} \eta_{\gamma\delta} + \ldots \quad (15)$$

where $C^{S}_{\alpha\beta\gamma\delta} = \frac{1}{V} \left(\frac{\partial^2 U}{\partial \eta_{\alpha\beta} \eta_{\gamma\delta}} \right)_{S,\eta'}$ and $C^{T}_{\alpha\beta\gamma\delta} = \frac{1}{V} \left(\frac{\partial^2 U}{\partial \eta_{\alpha\beta} \eta_{\gamma\delta}} \right)_{T,\eta'}$ are the second-order adiabatic and isothermal elastic constants, respectively. Of the three above approaches for obtaining elastic constants, approach (3) can be directly compared to analogous experiments, e.g., via Brillouin scattering experiments.

A topic that remains the subject of ongoing debate in the literature is the interpretation of elasticity theory at nonzero stress.[82–86] While the three above elastic constant definitions are equivalent in an unstressed crystal, their values differ under applied stress. Oganov proposes that part of the confusion in the literature surrounding this topic is due to their different definitions,[86] but it is also likely related to the lack of a unified and general interpretation of strain and stress at the atomic-level. Another question is how to handle the reference state with which to compare the stressed and strained state. Ray and Rahman suggested that the reference value of the simulation cell should be the average values obtained from a cell that is in the stress-free state.[87,88] However, Zhou and co-workers suggest that using such a reference value does not work properly

for a system with finite strain, and instead suggest that the reference parameters in simulations be the ones of the current state.[89–91]

2.2.3. Elastic Constant Calculations

Having briefly introduced the stress–strain conventions and their connection to mechanical properties in crystals, in the following sections we introduce common approaches (**Figure 3**) by which the most fundamental descriptor of elastic properties in MOF crystals is quantified: the elastic constant tensor.

Ab Initio Zero Kelvin Elastic Constants: Using DFT, elastic constants are commonly calculated using an energy-strain or stress–strain methodology that involves the deformation of the lattice-parameters of an energy-minimized structure by predetermined magnitudes. In practice, this is done by first performing an accurate energetic relaxation on the structure so that it reaches a state of near-zero stress. Following this structural relaxation, strain is applied to the structure's lattice vectors in the form of deformation gradients. The ionic degrees of freedom are then allowed to relax after these perturbations are applied, and the energy or stress of the systems are again calculated. The resulting elastic tensor can then be calculated using constitutive relations from linear elasticity. The stress–strain approach is implemented in DFT codes such as VASP[92,93] whereas the energy-strain method can be implemented in the CRYSTAL code.[94] Given the shallow potential energy surface of some MOFs,[95] extreme care should be taken in determining the appropriate deformation magnitudes for such calculations. These deformation gradients must be large enough to overcome the numerical noise in the energy calculations but also be small enough to stay within the valid elastic regime. When comparing elastic constant values across the literature, it should also be noted that its components depend upon the choice of coordinate system and lattice vectors. Given their well-studied experimental flexibility, the ab initio zero kelvin elastic tensor has been computed for a large number of Materials Institute Lavoisier (MIL) materials.[96–98,95]

Classical Force Field Zero Kelvin Elastic Constants: A particularly powerful approach for obtaining the elastic constant tensor at 0 K from classical simulations is to use the generalized Hessian matrix H. The generalized Hessian matrix is a $(3N + 6) \times (3N + 6)$ matrix, where N is the amount of atoms, defined by

$$H = \begin{pmatrix} H_{ij} = \dfrac{\partial^2 U}{\partial r_i \partial r_j} & H_{i\varepsilon} = \dfrac{\partial^2 U}{\partial r_i \partial \varepsilon} \\ H_{\varepsilon i} = \dfrac{\partial^2 U}{\partial \varepsilon \partial r_i} & H_{\varepsilon\varepsilon} = \dfrac{\partial^2 U}{\partial \varepsilon \partial \varepsilon} \end{pmatrix} \tag{16}$$

Here, $H_{\varepsilon\varepsilon}$ is the "Born" term that is the second derivative of the internal energy with respect to strain and $H_{\varepsilon i} H_{ij}^{-1} H_{i\varepsilon}$ is the "relaxation" term that accounts for the relaxation of atoms to

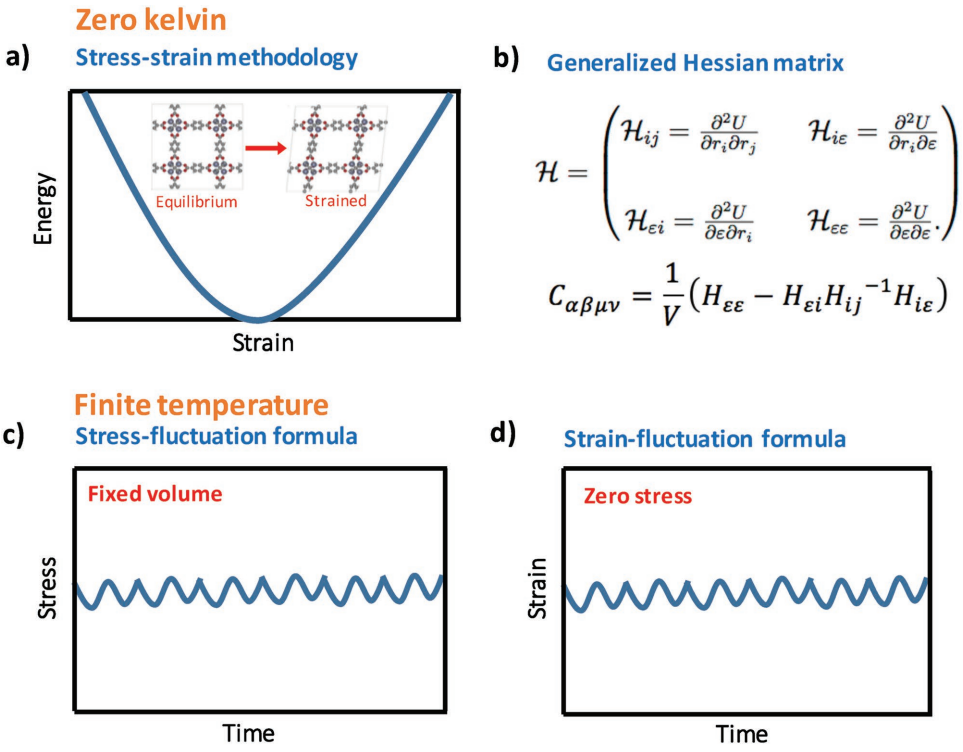

Figure 3. Schematics illustrating different computational approaches for calculating MOF elastic constant tensors. Zero kelvin approaches include: a) the energy–strain methodology involving deformations to the equilibrium lattice parameters, commonly used in ab initio calculations, and b) evaluation of the generalized Hessian matrix (second derivatives of internal energy), commonly used in classical simulations. Finite temperature approaches used in classical simulations include the: c) stress-fluctuation (fixed volume) and d) strain-fluctuation (zero stress) approach.

their zero-force position after a strain is applied. The elastic constants can then be obtained using the relationship[99]

$$C_{\alpha\beta\mu\nu} = \frac{1}{V}\left(H_{\varepsilon\varepsilon} - H_{\varepsilon i}H_{ij}^{-1}H_{i\varepsilon}\right) \tag{17}$$

Because Equation (16) requires knowledge of the second derivatives of internal energy, it is computationally expensive to evaluate using ab initio approaches. However, using classical simulations, it is trivial to accurately compute the generalized Hessian to arbitrary (machine) precision.

Analysis of the generalized Hessian also provides insight into an array of useful properties beyond the elastic tensor. For instance, for a given force field model, the generalized Hessian can be used to accurately optimize the atomic positions and size and shape of a unit cell, as well as perform a vibrational mode analysis of the system. Such analyses can be readily performed in simulation codes such as GULP[100] and RASPA[101] and are enabled via the implementation of a robust, mode-following "Baker's" energy minimization procedure.[102] In contrast to standard energy minimization methods based only on energies or forces (e.g., conjugate gradient minimizations), the Baker's approach computes the eigenvalues and eigenvectors of the generalized Hessian at each minimization step so that the eigenstates can be used to adjust all forces and their gradients to zero. Importantly, this ensures that all forces are zero and all eigenvalues are positive in the system. Negative eigenvalues would indicate saddle-points on the energy landscape, and this means that the structure is at a transition state on the verge of an atomic or unit cell change. In the Baker's minimization algorithm, the eigenvalues are shifted upward when needed to guarantee that a fully optimized state with all positive eigenvalues is attained.

We highlight the importance of the above Baker's minimization approach because it also provides valuable information for next-generation MOF flexible force field development efforts for two reasons. First, it enables the parameterization of physically meaningful force field models. Because the elastic tensor is known to correlate experimentally with a number of mechanical and thermal properties in materials,[38–43] it is logical that properly capturing the elastic constant tensor is also important to accurately predicting these same properties using a force field model. With this approach, a classical force field can be parameterized to ensure that it accurately describes the *ab initio* or experimental elastic constant tensor of a structure. As an example of how this can be implemented in practice, we refer to a recent case study of applying this procedure to create a MIL-47(V) [V^{IV}(OH)(BDC)] force field.[103] Second, it can assist in discerning physically unrealistic characteristics in existing force fields. For instance, if the Baker's minimization of a force field model causes significant structural deformations or a violation of the structure's expected symmetry, one immediately knows that there are force field parameters that should be adjusted in the model. Our experience with flexible force field models in the literature indicates that such inconsistencies are found in with a number of existing force field models.

Classical Force Field Finite Temperature Elastic Constants: There are two common approaches for measuring elastic constants in classical simulations at finite temperatures.[99,104–106] The first approach is performed at a fixed system volume and calculates the elastic constants using the stress-fluctuation formula

$$C_{\alpha\beta\mu\nu} = \frac{1}{V}\left\langle \frac{\partial^2 U}{\partial\eta_{\alpha\beta}\,\partial\eta_{\mu\nu}} \right\rangle - \frac{V}{k_B T}\left[\langle t^B_{\alpha\beta}t^B_{\mu\nu}\rangle - \langle t^B_{\alpha\beta}\rangle\langle t^B_{\mu\nu}\rangle\right] + C^K_{\alpha\beta\mu\nu} \tag{18}$$

whereas the second approach is performed in a system with variable volume but zero applied stress and uses the strain-fluctuation formula

$$C_{\alpha\beta\mu\nu} = \frac{k_B T}{V_0}\left[\langle \varepsilon_{\alpha\beta}\varepsilon_{\mu\nu}\rangle - \langle \varepsilon_{\alpha\beta}\rangle\langle \varepsilon_{\mu\nu}\rangle\right]^{-1} \tag{19}$$

Of these two approaches, the stress-fluctuation approach has the advantage that all the elastic constants can be calculated during a single simulation run and without performing any deformations to the system, and has faster convergence than the strain-fluctuation formula.[107] On the other hand, the advantage of the strain-fluctuation approach is that, for systems that show large-scale atomic rearrangements and changes in unit cell shape or size as a function of temperature, pressure, or loading, one need not identify the precise unit cell state that is required for the fixed-volume constraint of the stress-fluctuation approach. One open question for the strain-fluctuation approach is whether the V_0 reference state should be taken from the average volume at the conditions of interest or from the strain-free state at zero Kelvin. Furthermore, to more efficiently sample the greater phase space of systems in the strain-fluctuation approach, new methodologies are needed to facilitate faster property convergence. The stress-fluctuation, strain-fluctuation, and stress–strain methodologies were recently compared for fcc argon at 60 K and 1 bar.[108] For this simple system, the elastic tensors computed by these different approaches were in good agreement, with the notable exception of values calculated in the constant pressure isothermal–isobaric (NPT) ensemble, which showed a strong dependence on the barostat parameter that was chosen.

There are multiple sets of elastic constants that have been proposed, with those of Barron and Klein[109] and Wallace[81] being in in terms of Lagrangian strain while Marcus and Qiu[85] define theirs in Eulerian form. It is thus an open question whether there exists one fundamental set of elastic constants of the equilibrium state (stability condition, stress–strain relation, and elastic equations of motion). This calls for a detailed analysis of all these different expressions for elastic constants under load. Future work is needed to determine whether these expressions are truly different, or only different in their formulations. A starting point for performing this check would be to convert between the thermodynamic stress t and Cauchy stress σ using

$$t = \frac{\langle V\rangle}{V_0} h_0 \langle h\rangle^{-1}\sigma\langle h^T\rangle^{-1}h_0^T \tag{20}$$

where h_0 is the reference simulation cell, h^T is the transpose of h, and V_0 is the reference volume. Further simulations are also needed to elucidate what should be the correct reference state. Possible choices that include $h_0 = \langle h\rangle$ or taking h_0 as the strain-free state, but it might also include adapting the equation of motions.

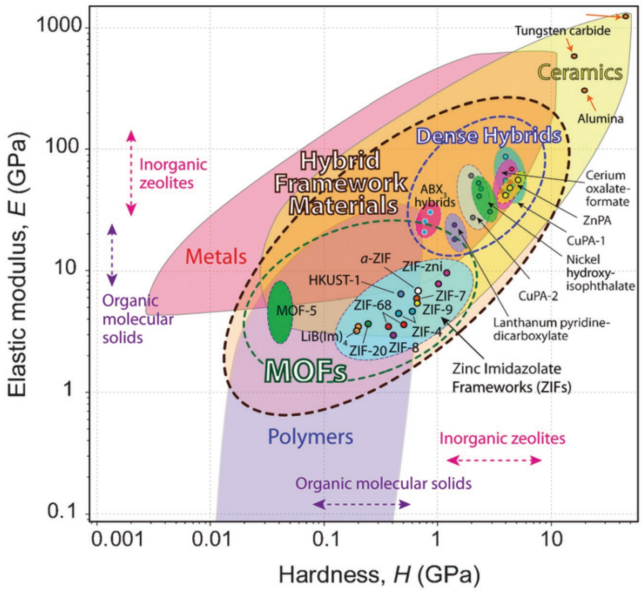

Figure 4. Property map illustrating the elastic modulus versus hardness properties of typical metal–organic frameworks relative to classical hard and soft materials. Reproduced with permission.[19] Copyright 2011, The Royal Society of Chemistry.

3. Structure–Property Relationships

Furthering our understanding of MOF structure-mechanical property relationships is critical to developing design criteria for the identification of structures with tailored mechanical properties. Such understanding would also help advance the opportunities and overcome the challenges discussed in section 4. The seminal review of Tan and Cheetham on this topic in 2011[19] provided some of the first broader insight into this topic area and put forth a basis for understanding the structure-property relationships governing the positioning of MOFs in the materials selection map shown in **Figure 4**. The intention of this section is not to cover the same ground, but rather to highlight recent advances in structure-property relationship understanding in emerging areas that were not well-established at the time of their review, including the role of characteristics such as linker effects, defects, and interpenetration.

3.1. Linker Effects: Electronics and Flexibility

The elastic and bulk moduli of the zeolitic imidazolate framework (ZIF) family has previously been shown to be dependent upon metal center identity, linker length, and pore volume.[19] However, recent reports have also investigated the extent to which electronic linker effects dictate their mechanical response. Li and co-workers contrasted the framework rigidity of ZIF-8 with the isostructural metal azolate framework MAF-7 [$Zn(mtz)_2$], where mtz = 3-methyl-1,2,4-triazolate. Both structures contain tetrahedral coordinated Zn^{2+}, with coordination arising from N atoms in the 2 and 4 positions. The additional N atom in the mtz ligand remains noncoordinating, and the cubic sodalite topology is adopted in each case.[110] Values for E_{max} and E_{min}, alongside G_{max} and G_{min}, were calculated (and the former confirmed by nanoindentation measurements) to be ≈20% and 3% higher for the triazolate based structure. High-pressure powder diffraction measurements also illustrated MAF-7 to be less compressible than ZIF-8 (10.8 and 6.52 GPa, respectively). These effects were all ascribed to the additional electron donating N atom in the triazolate ligand, which resulted in a stronger Zn–N interaction. This theory was consistent with the shorter Zn—N bond distance in MAF-7 of 1.98 Å, compared to 1.983 Å in ZIF-8.

A similar general effect was witnessed in the UiO family (**Figure 5**) by Maurin and co-workers. In an ideal UiO-66 crystal structure, Zr^{4+} octahedral clusters are connected to neighboring clusters via twelve BDC linkers, in a face-centered cubic (fcu)

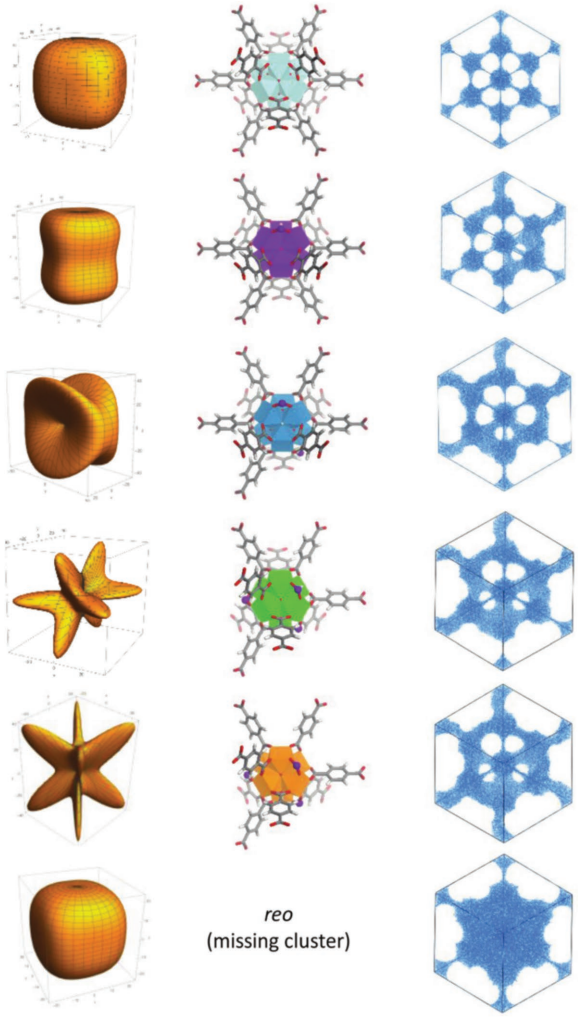

Figure 5. Snapshots of calculations for the spatially dependent Young's modulus and porosity in defective UiO-66 structures. Defects are shown from the perspective of a single cluster where additional linkers are consecutively removed, except for the reo structure that is also missing a cluster. Porosity available for adsorption is shown in blue for a probe diameter of 3 Å. Each missing ligand is replaced with either formate, acetate, chloride trifluoroacetate, or hydroxide ions. Each cluster is colored according to its coordination number: 12, light blue; 11, purple; 10, dark blue; 9, green; and 8, orange. Reproduced with permission.[119] Copyright 2016, The Royal Society of Chemistry.

arrangement. The high network connectivity of UiO-66 has led to calculated *B*, *E*, and *G* values of 40, 47, and 18 GPa, respectively, placing UiO-66 in the upper limits of those reported for MOFs.[111] An experimental bulk modulus of 17 GPa was identified, along with a value of 25 GPa for an isostructural variant, UiO-66-NH_2, containing a mono amine-functionalized benzene dicarboxylate ligand. Here, the authors ascribed the lower compressibility to steric hinderance and the formation of intraframework H bonds in the amino functionalized derivative. Complimentary experiments on MIL-125(Ti) and its amino functionalized counterpart yielded similar results, with bulk moduli of 10 and 13 GPa, respectively.[49]

Hobday et al. calculated the full elastic tensors of UiO-67, which is an expanded version of UiO-66, with a 4,4′-biphenyl dicarboxylate (bpdc) linker. Average bulk and Young's moduli of 17.4 and 24.1 GPa were extracted, with the latter confirmed by nanoindentation.[112] The results displayed an expected reduction from the values of ideal UiO-66, confirming the correlation of increasing linker length and decreasing elastic moduli. A derivative, with replacement of bpdc by 4,4′-azobenzene dicarboxylate (abdc) was also synthesized and investigated. Molecular dynamics calculations revealed abdc ligands to "bow" out of plane in the crystal structure, while the bpdc ligands remained approximately planar. The similar solvent accessible volumes of the two frameworks (66% and 72%) allowed the authors to draw conclusions on the geometry of the linker upon mechanical response. A decrease in calculated bulk modulus to 15.2 GPa was observed (and confirmed by high-pressure powder diffraction experiments), with calculated and experimental decreases in *E* of between 10% and 35% recorded. Given that similar decreases in *E* in other MOF families were only witnessed with changes in framework porosity of ≈40%, the effects were ascribed to the bowed, flexible nature of the abdc ligand.

The study of collective low frequency vibrations in the terahertz domain in MOFs is a relatively new area of investigation, and has been connected to several aspects of flexibility including gate-opening, shear deformations, amorphization, and breathing.[113] Recently, Tan and co-workers studied the MIL-140A framework using inelastic neutron scattering, synchrotron radiation far-infrared spectroscopy, and Raman spectroscopy, probing different physical behavior such as coordinated shearing dynamics, cooperative "trampoline-like" motions, and hindered rotational organic linker movements.[114] While not trivial, extension of this technique across further MOF systems will prove an important area going forward, given the links between the motions uncovered and behavior such as negative thermal expansion and structural collapse.[98]

3.2. Defects and Elasticity

The occurrence of different defect types in the UiO-66 family (Figure 5) of MOFs has been widely reported.[115,116] Notably, missing clusters[117] have been identified in the structure by Cliffe et al., who linked diffuse scattering from UiO-66(Hf) to that predicted for a structural model including correlated vacancies at $[Hf_6O_4(OH)_4]$ cluster sites. In this latter model of reo topology, 8% of cluster sites are vacant. Values for B, *E*, and *G* of ≈18, 23, and 9 GPa calculated for this defective scenario represented a decrease of over 50% from the idealized framework.

Observations on the relatively high bulk modulus of pristine UiO-66(Zr) were confirmed by Van Speybroek and co-workers, who calculated the bulk modulus as 38 GPa and subsequently investigated the effect of a different type of defect, missing linkers, upon *B*.[118] Here, several models missing 1 and 2 linkers per cluster were constructed and bulk moduli were calculated. The lowering of the Zr-cluster coordination number to 11 (i.e., the introduction of 1 missing linker defect per cluster) resulted in a reduction in *B* to 25–31 GPa, depending upon the linker choice, while further reductions to coordination numbers of 10 led to further decreases in *B* between 16 and 22 GPa.

Coudert and co-workers increased considerations of missing linker defect-induced elasticity in UiO-66 to include minimum and maximum values for *E* and *G*.[119] The largest reduction in each case was observed for minimum values upon initial removal of one linker per cluster, before successive further incorporation of 2, 3, and 4 missing linker defects yielded decreasing relative reductions in E_{min} and G_{min}. Values were however found to be dependent on the replacement moiety, e.g., formate or acetate. Interestingly, a negative Poisson's ratio was observed in some cases, while CO_2 uptake at low pressures was adversely affected by the presence of defects, although high pressure uptake was greater in nonperfect structures.

A rare study outside of the UiO family can be found in the MUF-32 MOF.[120] The structure consists of three ligands (dabco, 4,4′-bipyridyl (bipy) and 4,4′,4″-nitrilotribenzoate (ntb)), though the latter two are described to be decorative in a unit cell of formula $[Zn_2(ntb)_{4/3}(bipy)_{1/2}(dabco)_{1/2}]$. *E* and *G* were calculated as 5.24 and 1.84 GPa. Removal of bipy ligands by heating yielded a structurally identical framework of $[Zn_2(ntb)_{4/3}(dabco)_{1/2}]$ composition, while further heating in vacuo enabled dabco removal and left only ntb ligands in the framework. Decreases in *E* and *G* to 2.89 and 0.99 upon bipy removal were observed, before the final $[Zn_2(ntb)_{4/3}]$ was calculated to possess extremely low values of 1.60 and 0.54 GPa, respectively.

3.3. Defects and Amorphization

The decrease in *G* found upon defect introduction has consequences not just for the elasticity of MOFs but also for the conditions at which structural collapse, or amorphization, occurs.[121] Experimentally, ZIF-8 was observed to undergo irreversible pressure-induced amorphization (P_A) at 0.34 GPa,[51] proposed to be a consequence of the softening of its shear modulus.[122] Separately, the calculated *P*(*V*) profile of defect-free UiO-66 and UiO-67 was observed to contain maxima at 1.83 and 0.45 GPa, at which point further decreases in internal pressure yielded decreases in the constrained unit cell volume.[123] Evaluation of the three independent elastic constants with pressure showed violations of one of the three associated Born stability criteria at near identical pressures, which also agrees well with reported experimental results of P_A.[49,112] It would therefore be expected that construction of calculated *P*(*V*) profiles for successive missing-linker UiO systems (of lower shear moduli) would yield lower values of P_A. This was confirmed by

Van Speybroek and co-workers, with reductions from 1.83 to 1.35 GPa for UiO-66.[123]

Bennett et al. considered the structural mechanism of amorphization in UiO-66, connecting the successive introduction of "missing-linker" defects by ball-milling to the disappearance of Bragg diffraction and porosity.[124] A combination of solid state nuclear magnetic resonance, infrared spectroscopy, and pair distribution function studies showed the coordination bonds between Zr_6 clusters and benzenedicarboxylate ligands to break upon successive ball-milling times.

3.4. Interpenetration and Elasticity

The large porosity of MOFs occasionally results in the growth of one lattice within another to yield doubly or triply interpenetrated structures[125] which possess lower porosities, greater densities, and distinct structural and gas adsorption characteristics. Partial interpenetration, where one sublattice is fully occupied and another displays an occupancy of less than unity, remains a rare occurrence in the literature.[126] A ligand based on biphenyl-4,4′-dicarboxylic acid, with a phenyl substituted diazocine functional group bridging the 2,2′positions, forms a structure in a primitive cubic topology when combined with Zn_4O secondary building units. Telfer and colleagues showed that while reaction in *N*,*N*-dibutylformamide yielded the nonpenetrated α-MUF-9 phase, reaction in DMF resulted in a doubly interpenetrated structure, termed the β-MUF-9 phase. Elastic properties were calculated for both structures, resulting in increases in average *B*, *E*, and *G* upon interpenetration (6.8, 3.7, and 1.3 GPa for α-MUF-9 and 11.7, 8.9, and 3.2 GPa for β-MUF-9). Interestingly, the occupancy of the second sublattice could be controllably altered in the range between 0 and 1 using different solvent mixtures during synthesis, yielding partially interpenetrated structures (PIP-MUFs).

4. Mechanical Property Implications for MOF-Enabled Technologies

In this section, we identify what we consider to be key opportunity areas and challenges from an applications perspective that originate from MOF mechanical properties, with the goal of stimulating further research in these critical areas. For the opportunity areas, we highlight case studies in the fields of sensing devices, gas separations, and storage where the connection between promising application performance and MOF mechanical properties is evident. In many cases, a reversible phase transition is at the heart of the promising application performance, and it has been shown that mechanical properties such as the elastic tensor can be a strong predictor of whether such structural transitions can occur.[96] On the other hand, we also discuss challenges that can arise in different application scenarios, such as the deployed MOF being able to withstand pore collapse or amorphization due to mechanical loadings (e.g., bending, torsion, and compression) and postprocessing techniques such as ball-milling[127,128] and compression into shaped forms.

4.1. Opportunity Areas

4.1.1. Microcantilever Sensors

Selectivity for the analyte of interest remains a major challenge in the development of next-generation chemical sensors, with performance improvements (along with reductions in their size and cost) creating exciting possibilities for widely deployed distributed sensor networks[129] in applications such as wearable technologies and air pollution management.[130] MOFs can offer improvements over state-of-the-art chemical sensing materials due to the analyte selectivity imparted by their precisely tuned pore environments. One highly sensitive sensor design, microcantilevers (**Figure 6**),[131] detects mass uptake by induced stress at the interface between the cantilever beam surface and its selective chemical coating. By utilizing either a dynamic or static transduction mechanism, mass detection on the sub-ng scale can be achieved.[132,133] Whereas dynamic microcantilevers rely upon changes in the resonant frequencies of an oscillating cantilever beam to detect analyte adsorption, static microcantilevers rely upon quantifying the beam deflection.

Allendorf et al. first demonstrated that an CuBTC (Cu_3[benzene-1,3,5-tricarboxylate]$_2$) thin film deposited on a static silicon microcantilever with a built-in piezoresistive sensor can serve as a sensitive and selective sensor for the detection of water vapor.[134] It was subsequently demonstrated that this MOF can also be used for the detection of various volatile organic compounds.[135,136] The mechanical properties of CuBTC are critical to this application as they dictate the adsorbate-induced changes in lattice parameters that create the detected microcantilever stress. While microcantilevers have since been fabricated using the ZIF-8[137] and MIL-53(Al) (Al(OH)BDC)[138] structures, exploring the detection responses of MOFs with increased Young's moduli[139] and larger-scale guest-induced structural changes would further push the limits of microcantilever sensitivity possibilities.

4.1.2. Gas Separations and Storage

MOFs have been widely studied for their potential applications in gas separations and storage, with the majority (≈50%) of MOF-related patents claiming industrial use having been filed in this area as of 2015.[12] A strong motivator for such applications is the role that MOFs could play in accelerating progress toward an energy economy that greatly reduces our greenhouse gas emissions by easing our reliance on fossil fuels. One proposed route for achieving this is to use MOFs for methane storage as a short-term transitional fuel, hydrogen storage as a long-term fuel, and for CO_2 capture as an immediate action to mitigate climate change impacts.[140]

Natural gas has economic and environmental advantages over traditional petroleum sources for on-board vehicular fuel storage applications, but suffers from a relatively low volumetric energy density. In a significant breakthrough in this area, Long and co-workers demonstrated that the flexible compounds Fe(bdp) and Co(bdp) (bdp = 1,4-benzenedipyrazolate) undergo phase transitions at targeted methane pressures to produce adsorption and desorption isotherms that exhibit a distinct "S-shape"

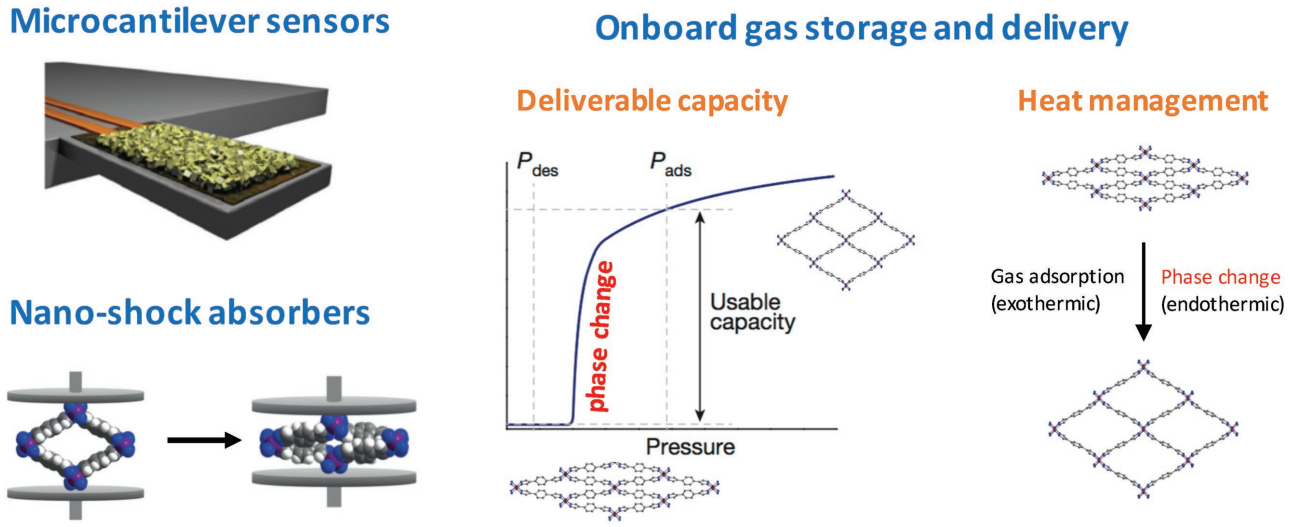

Figure 6. Selected areas where MOF mechanical properties have presented exciting opportunities for technological applications. Top-left image: Adapted with permission.[17] Copyright 2017, The Royal Society of Chemistry. Bottom-left and right-hand images: Adapted with permission.[147] Copyright 2015, Nature Publishing Group.

(Figure 6).[141] Importantly, these results showed that MOF flexibility can be exploited to produce deliverable methane storage capacities that are greater than what was previously deemed possible in conventional structures[142] while simultaneously addressing heat management issues that inherently arise from adsorption and desorption processes. The mechanical origin of the exceptional methane working capacity of the structure is due to the free energy for a reversible structural phase transitions occurring near the appropriate lower and upper pressures for practical methane storage applications (near 5.8 and 35–65 bar, respectively); the effective heat management characteristics are due to the enthalpy change associated with its structural phase transition, which largely offsets its exothermic enthalpy of adsorption during methane adsorption (and vice versa for endothermic desorption), thus minimizing the magnitude of heat effects which traditionally reduce the working capacity of adsorbent materials. The large volume change associated with the material's phase transitions, however, may create practical challenges for volume-limited storage tank applications.

More efficient separation technologies are an area where significant global energy savings can be achieved. It has been estimated that 5–15% of energy consumption in the U.S. is used by industrial fluid separation processes, with thermally driven separations accounting for 80% of this total.[143,144] Thermally driven separation technologies such as distillation rely upon component phase changes to separate one species from another, resulting in a process that is inherently energy-intensive. Adsorbents can serve as clean energy alternatives to these separations by exploiting a fundamentally different separation mechanism, thus allowing certain separations to be performed at lower operating costs than thermally driven processes.[145] Kitagawa and co-workers elegantly demonstrated that the soft porous crystal Cu(aip) (aip = azidoisophthalate) can be utilized to selectively capture and subsequently oxidize CO to CO_2 from a mixture containing N_2.[146] This separation is otherwise energetically intensive to perform, with state-of-the-art approaches requiring the chemisorption of CO on transition metal surfaces. Through a combination of specific weak adsorption interactions followed by a cooperative structural transformation, however, a so-called "self-accelerating" CO adsorption phenomenon results whereby increasing amounts of CO can be accommodated due to the flexible expansion of narrow channels in the structure. In subsequent work, a significant breakthrough for CO_2 capture technologies was demonstrated via the cooperative insertion of CO_2 in a series of "phase-change" materials of the formula mmen-M_2(dobpdc) (M = Mg, Mn, Fe, Co, Zn, mmen =*N,N*′-dimethylethylenediamine, dobpdc = 4,4′-dioxidobiphenyl-3,3′-dicarboxylate). It was shown that energy-efficient CO_2 capture from N_2 under representative flue gas compositions from temperature swing adsorption cycles could be achieved in these materials.[147]

4.2. Application Challenges

4.2.1. Electronic Devices and Sensors

There is a strong impetus in the microelectronics industry to transition from inorganics toward organic-based materials, driven by factors such as lower cost, greater functional complexity, and prospects for downsizing devices toward Moore's law. The majority of MOFs are electrical insulators, but design strategies for synthesizing electronically conductive MOFs have emerged in the past few years.[148] While electronic conductivity is not a prerequisite for all MOF-enabled devices (e.g., in cases where the MOF serves as chemically selective sensing layers), this property is critical to the exploitation of MOFs in applications such as digital circuits and thermoelectric devices. Strategies for designing electronically conductive MOFs include through-bond conduction, through-space conduction,[148] and conduction facilitated by guest molecules.[149] Numerous challenges must still be overcome, however, before MOFs become widespread in commercial electronics applications. A high-level

roadmap for addressing the broader array of challenges associated with integrating MOFs with electronic devices and sensors is discussed in a recent comprehensive review;[17] our focus here is only to present some of the key challenges in the context of MOF mechanical properties.

From a device fabrication standpoint, the mechanical property requirements that must be met will depend upon the stage at which the MOF is incorporated into the device. Microfabrication processes, such as those used for integrated circuits, can be summarized by the following sequence of operations: thin film deposition, patterning, doping, and etching. In such a process, summarized in **Figure 7**a, whether the MOF is incorporated in the final stage and then exposed to the environment, e.g., as a chemical sensing layer, or earlier on in the process, e.g., as an interlayer dielectric layer, will present different mechanical stability demands. For instance, wear resistance to abrasion will be relevant in cases where the MOF coating is exposed to uncertain environmental conditions. Nanoscratching is an established technique for measuring this property, and can also provide insight into adhesion properties via the applied strength required for delamination.[150–152] This characterization approach was applied to several dense, electrochemically grown MOF thin films and it was found that Cu(CHDA) (CHDA = trans-cyclohexane-1,4-dicarboxylate), the structure with the highest Young's modulus and hardness (10.9 and 0.46 GPa, respectively), had the best scratch and wear resistance and exhibited an elastic recovery that is comparable to that of organic polymers and nanocomposites.[59] The material with the lowest Young's modulus and hardness (0.8 and 0.02 GPa, respectively), $Cu(INA)_2$ (INA = isonicotinate), exhibited an elastic recovery that is comparable to that of a scratched zeolite mordenite framework inverted (MFI) film.

MOFs generally exhibit a lower hardness than pure inorganics and will therefore require additional caution in any postprocessing fabrication steps. Furthermore, when MOFs are incorporated into devices via a layer-by-layer microfabrication process, attention should be paid to the resulting interfacial strains that can result between layers. Tensile strain from mechanical stress, for instance, can lead to device failure via film debonding or cracking.[60] Bending tests to evaluate such effects have been performed on memory resistors using Au/CuBTC/Au[61] and Ag/ZIF-8/Au[62] on PET (PET = polyethylene terephthalate). Promisingly, the authors noted that in these cases, the conformable nature of the MOF film resulted in device performances under bending conditions that would be difficult to obtain with their purely inorganic counterparts.

Yet to be determined, however, are the implications of MOF responses to temperature and guest-induced stimuli on device stability characteristics. In these cases, the resulting change in lattice parameters can cause strain between the MOF and its interfaced layers. Changes in temperature, for example, can cause residual stresses due to differences in the coefficient of thermal expansion of the MOF and its substrate which can cause cracking, buckling or film delamination (Figure 7b).[153] While common electronic device substrates such as copper, aluminum, and silver exhibit positive thermal expansion,[154,155] negative thermal expansion is expected in a number of MOFs, including the well-studied CuBTC structure.[156–159] Given the temperature changes that will take place during MOF film growth and processing, such effects should be taken into account. Furthermore, during the operation of sensors such as microcantilevers, temperature fluctuations can create interfacial stresses that complicate the expected sensor response.[160]

4.2.2. Gas Separation and Storage

An early perceived hurdle for the application of MOFs in gas separation and storage applications was their degree of stability in the presence of moisture. Building off the findings of studies dating back to the early 2000's, design strategies have since been identified for improving MOF chemical stability via structural factors such as ligand functionalization,[161,162] hydrophobicity,[163,164] and metal-ligand coordination bonds that are

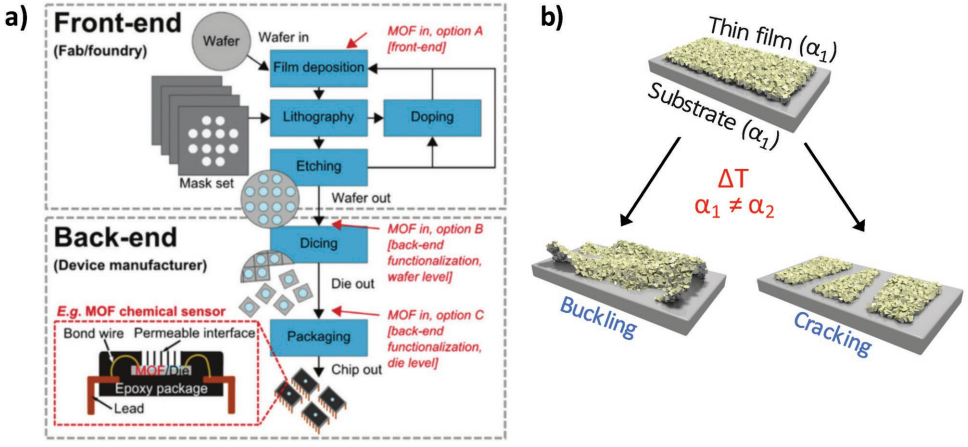

Figure 7. a) Unit operations of microfabrication and chip production. Three options for MOF integration during the production of a hypothetical complementary metal-oxide-semiconductor fabricated chemical sensor are proposed: in the course of the microfabrication process (option A), before dicing step in back-end processing (option B), and on individual dies before packaging (option C). b) Example effects of residual stress on film properties due to a mismatch in the thermal expansion coefficient, α, of the film and its substrate caused by variations in temperature during MOF film processing and device operation. Adapted with permission.[17] Copyright 2017, The Royal Chemical Society.

inert toward water.[165,166] As a result of these efforts, there now exists a large number of hydrothermally stable structures that maintain their crystallinity and surface area even in acidic and basic solutions.[167] This same degree of understanding is not yet present for MOF mechanical properties due to the relatively fewer characterization studies that have been performed; this is likely because of the relative inaccessibility of the required characterization equipment (compared to more simple water exposure apparatuses) and, in some cases, the large single crystals needed for characterization. Nonetheless, the number of mechanical characterization studies is steadily growing, with their importance underscored by the role mechanical properties will play in dictating the changes that MOFs undergo as they are processed from their as-synthesized to their application-ready form.

In gas separation and storage applications, the as-synthesized material will be engineered into forms that can include pellets or granulates (often compressed with the aid of binders or lubricants), mixed-matrix membranes, or monolith-based structures. While fixed beds are often utilized to evaluate MOF separation performance in laboratory environments, monoliths are more practical solutions due to their improved mass and heat transfer characteristics and lower pressure drops at high flow rates.[168] Amine-functionalized MOF films of mmen-M_2(dobpdc) (M = Mg and Mn) supported on monolith contactor substrates have been investigated for CO_2 capture from simulated flue gas, and producing MOF coatings with suitable mechanical adhesion properties to withstand the activation heating treatment was found to be a challenge.[169] In this regard, the low coefficient of thermal expansion of cordierite makes it an attractive material for monoliths to help avoid film delamination issues similar to those shown in Figure 7b. Kaskel and co-workers presented the first purely MOF-based monolith consisting of CuBTC via an extrusion process with methyl hydroxyl propyl cellulose and methoxy functionalized siloxane ether as additives.[170] This monolith exhibited impressive mechanical properties, with a crushing strength of 320 N (roughly 3× that of a cordierite commercial honeycomb) after activation.

Mixed matrix membranes can combine the processability of polymers with the separation properties of MOFs and are particularly attractive as energy-efficient and scalable separation technologies.[171] Given that many of the flexibility-driven adsorption behaviors of MOFs have been observed in their single crystal or powder forms, the implications of incorporating MOFs into composite polymer systems remain an important open question. In a recent theoretical study addressing this topic, MOF particles incorporated into mixed matrix membranes of varying properties were modeled using finite element methods to predict their resulting macroscopic properties.[172] The variation in the effective bulk modulus of the adsorbent due to varying thicknesses and encapsulating matrix properties were quantified and it would found that, even for very soft matrix polymers which are softer than the adsorbent itself, an increase in the effective bulk modulus of the adsorbent results. Future work exploring the conditions under which flexibility-induced characteristics such as the gate opening and breathing behaviors observed in MOFs can be retained in their polymer matrix form would be of great interest to the adsorption community.

Natural gas and hydrogen storage for onboard fuel tanks are volume-limited applications that will require some degree of shaping of the MOF from its as-synthesized form. This densification can compromise the porosity, crystallinity, and gas storage characteristics of the material. For instance, while CuBTC is a top performing material for room-temperature volumetric methane storage, compacting it into wafers was shown to drastically decrease its capacity due to partial structural collapse.[173] In an early study with hydrogen storage implications, Müller and co-workers explored the effects of powder densification on the hydrogen storage capabilities of MOF-5,[174] determining the optimal material density to be ≈0.5 g cm^{-3}. Higher densities than this lead to large reductions in the pore volume and surface area, as well as amorphization, decreasing its gravimetric excess capacity. An extensive recent study by Llewellyn and co-workers studied the effects of shaping powders of UiO-66(Zr), UiO-66(Zr)-NH2, MIL-100(Fe), MIL-127(Fe) into spheres using a polyvinyl-based binder.[175] Based on the adsorption isotherms and enthalpies of adsorptions for eight different gases (N_2, CO, CO_2, CH_4, C_2H_6, C_3H_8, C_3H_6, C_4H_{10}), while the gravimetric uptakes for the materials decreased in the sphere versus powder form, the volumetric uptake based on the bulk density showed an opposite trend. The appropriate degree of densification for a given storage application will likely be dictated by the trade-off in porosity and crystallinity characteristics caused by compression and will thus depend strongly on the mechanical properties of the structure; this further underscores the importance of additional characterization studies to unravel mechanical structure-property relationships in MOFs.

5. Concluding Remarks

In their review on "soft porous crystals" in 2009,[20] Kitagawa and co-workers presented visionary perspectives on the role that MOF flexibility may play in its future technological applications. At the time of their review, a number of the proposed MOF flexibility characteristics had been studied at the fundamental level, but convincing demonstrations of their utility for practical applications were lacking. Focused effort to understand MOF mechanical properties has significantly progressed since then and, as highlighted in this review, brought to fruition several demonstrations of their importance for practical applications.

Given the breakthrough for methane storage applications demonstrated by Long and co-workers,[141] the question of whether MOF flexibility can also be exploited to enable exceptional working capacities for hydrogen storage technologies is warranted. Hydrogen is a more weakly interacting species than methane, however, and the challenge lies in identifying a MOF with a high volumetric hydrogen capacity that also has an appropriate structural free energy difference to facilitate a hydrogen-induced phase transition that: (1) occurs at commercially relevant pressures and temperatures for hydrogen fueling station technologies (e.g., suitable for a 5 to 100 bar pressure swing cycle), and (2) lacks a broad hysteresis[176] that would reduce its working capacity during cyclic adsorption/desorption cycles.

Another area where significant MOF-enabled technological breakthroughs have not yet been realized, but which we believe to be promising, is in the realm of thermoelectric devices. A defining structural feature of MOFs that is absent from the traditional material classes that have been explored for thermoelectric device applications, namely organic polymers and inorganic seminconductors, is the combined nanoporosity and long-range crystallinity that allows unprecedented opportunities for minimizing thermal conductivity while maximizing electrical conductivity properties. While these two properties are highly correlated in most materials, MOFs may present an exception. The nanoporosity and mechanically flexible nature of MOFs can lead to scattering in the heat-carrying phonons to impart low thermal conductivity properties, whereas their long-range order can facilitate charge mobility.[177] The pore space of MOFs can also be used for the infiltration of guest molecules that can significantly enhance properties that include the electronic conductivity,[178] as demonstrated by the six order of magnitude improvement for TCNQ@CuBTC (TCNQ = tetracyanoquinodimethane),[149] among other properties.

Other application areas where the benefits of MOF mechanical properties could be utilized are for their use in flexible electronics or as nanosprings for shock absorption and dissipation. The promising device performances of ZIF-8 and CuBTC MOFs during bending tests[61,62] hint that their elasticity may make them suitable for flexible electronics, which is attractive given the growing demand for small and robust sensors for applications such as distributed sensor networks and wearable technologies. We are also intrigued by recent prospects of MOFs for shock absorption and dissipation applications,[180,181] including an exciting recent study that showed the per gram energy absorption for UiO-type MOFs at compressive stresses greater than 2 GPa is similar to the amount of energy that is released in the explosion of trinitrotoluene (TNT).[182]

In reviewing computational methods for calculating the elastic constant tensor, we brought to light open questions related to the calculation of mechanical properties in crystalline materials. Key points that should be taken into account when interpreting elasticity theory at nonzero stress include recognition of the fact that there are various definitions for elastic constants, and while these are equivalent in an unstressed crystal, their results differ under applied stress. Also important to note is that commonly used expressions[99] for stress and elastic constants in terms of potential energy interactions and their derivatives are derived under the assumption that strain is infinitesimal and homogeneous. Thus, when modeling MOFs that exhibit large-scale flexibility, the results of these stress calculations should be interpreted with caution. We are nonetheless enthusiastic, however, about the possibilities enabled by large-scale computational data sets such as those in the CoRE database;[183,184] by computing the elastic constants for these structures, unprecedented opportunities for elucidating large-scale mechanical property-structure relationships and the testing of theories through machine learning and genetic algorithms becomes possible.

It is also clear that whether a particular MOF mechanical property presents an opportunity or challenge for a given application can be highly case-specific. One can look at the mechanical properties that lead to their pressure-induced amorphization as one such example. In scenarios such as post-processing ball milling or shaping, pressure-induced amorphization can be a challenge that inhibits the material's application prospects by yielding a less porous structure.[121] In some instances, structural collapse has been utilized to yield liquids and glasses which retain the chemical components and connectivity of crystalline MOFs.[185,186] The study of the fundamental properties of such MOF-glasses, or MOF-liquids,[187] will prove important in the future. Additionally, the structural instabilities leading to collapse can be exploited in gas storage applications as a strategy for the irreversible capture of hazardous molecules by collapsing the framework around the guest species.[188,189] Further complicating the interpretation of mechanical property implications for practical applications are the significant changes that can occur when the as-synthesized material is converted to its application-relevant form. While such effects have only been studied in a limited number of MOFs, the impacts can be significant. For instance, when confined to a thin film[190] or synthesized below a critical particle size,[191] significant alterations to MOF phase transition behaviors have been observed. Overall, the complexity of the many open questions that remain in this field and their direct connection to important opportunity areas and challenges for MOF applications suggests that investigations into MOF mechanical properties will continue to be a rich area of research moving forward.

Acknowledgements

The authors thank Jon Zimmerman for fruitful discussions regarding stress–strain relationships and mechanical properties in crystals. N.C.B. acknowledges the support of the Sandia National Laboratories Truman Fellowship Program and N.C.B. and M.D.A acknowledge support by the Sandia National Laboratories Laboratory Directed Research and Development (LDRD) Program. Sandia National Laboratories is a multimission laboratory managed and operated by National Technology and Engineering Solutions of Sandia, LLC., a wholly owned subsidiary of Honeywell International, Inc., for the U.S. Department of Energy's National Nuclear Security Administration under contract DE-NA0003525. D.D. would like to thank The Netherlands Research Council for Chemical Sciences (NWO–CW), through a VIDI grant, and T.D.B. would like to thank the Royal Society for a University Research Fellowship, and for their support.

Conflict of Interest

The authors declare no conflict of interest.

Keywords

defects, electronic devices, mechanical properties, metal–organic frameworks, sensors

Received: July 23, 2017
Revised: September 11, 2017
Published online: November 17, 2017

[1] B. F. Hoskins, R. Robson, *J. Am. Chem. Soc.* **1989**, *111*, 5962.
[2] H.-C. Zhou, S. Kitagawa, *Chem. Soc. Rev.* **2014**, *43*, 5415.

[3] S. Kitagawa, R. Kitaura, S. Noro, *Angew. Chem., Int. Ed. Engl.* **2004**, *43*, 2334.
[4] G. Férey, C. Mellot-Draznieks, C. Serre, F. Millange, J. Dutour, S. Surble, I. Margiolaki, *Science* **2005**, *309*, 2040.
[5] H. Furukawa, K. E. Cordova, M. O'Keeffe, O. M. Yaghi, *Science* **2013**, *341*, 1230444.
[6] P. Li, N. A. Vermeulen, C. D. Malliakas, D. A. Gómez-Gualdrón, A. J. Howarth, B. L. Mehdi, A. Dohnalkova, N. D. Browning, M. O. Keeffe, O. K. Farha, *Science* **2017**, *356*, 624.
[7] T. C. Wang, W. Bury, D. A. Gómez-Gualdrón, N. A. Vermeulen, J. E. Mondloch, P. Deria, K. Zhang, P. Z. Moghadam, A. A. Sarjeant, R. Q. Snurr, J. F. Stoddart, J. T. Hupp, O. K. Farha, *J. Am. Chem. Soc.* **2015**, *137*, 3585.
[8] S. S.-Y. Chui, S. M.-F. Lo, J. P. H. Charmant, A. Guy Orpen, I. D. Williams, *Science* **1999**, *283*, 1148.
[9] R. Vaidhyanathan, S. S. Iremonger, G. K. H. Shimizu, P. G. Boyd, S. Alavi, T. K. Woo, *Science* **2010**, *330*, 650.
[10] S. M. Cohen, *Chem. Rev.* **2012**, *112*, 970.
[11] P. Z. Moghadam, A. Li, S. B. Wiggin, A. Tao, A. G. P. Maloney, P. A. Wood, S. C. Ward, D. Fairen-Jimenez, *Chem. Mater.* **2017**, *29*, 2618.
[12] H. Furukawa, U. Muller, O. M. Yaghi, *Angew. Chem., Int. Ed.* **2015**, *54*, 3417.
[13] M. D. Allendorf, V. Stavila, *CrystEngComm* **2014**, *17*, 229.
[14] T. Faust, *Nat. Chem.* **2016**, *8*, 990.
[15] J.-R. Li, R. J. Kuppler, H.-C. Zhou, *Chem. Soc. Rev.* **2009**, *38*, 1477.
[16] M. D. Allendorf, A. Schwartzberg, V. Stavila, A. A. Talin, *Chem. - Eur. J.* **2011**, *17*, 11372.
[17] I. Stassen, N. Burtch, A. Talin, P. Falcaro, M. Allendorf, R. Ameloot, *Chem. Soc. Rev.* **2017**, *46*, 3185.
[18] A. J. Howarth, Y. Liu, P. Li, Z. Li, T. C. Wang, J. T. Hupp, O. K. Farha, *Nat. Rev. Mater.* **2016**, *1*, 15018.
[19] J. C. Tan, A. K. Cheetham, *Chem. Soc. Rev.* **2011**, *40*, 1059.
[20] S. Horike, S. Shimomura, S. Kitagawa, *Nat. Chem.* **2009**, *1*, 695.
[21] A. Schneemann, V. Bon, I. Schwedler, I. Senkovska, S. Kaskel, R. A. Fischer, *Chem. Soc. Rev.* **2014**, *43*, 6062.
[22] F.-X. Coudert, *Chem. Mater.* **2015**, *27*, 1905.
[23] S. S. Nagarkar, A. V. Desai, S. K. Ghosh, *Chem. Asian J.* **2014**, *9*, 2358.
[24] Y. Sakata, S. Furukawa, M. Kondo, K. Hirai, N. Horike, Y. Takashima, H. Uehara, N. Louvain, M. Meilikhov, T. Tsuruoka, S. Isoda, W. Kosaka, O. Sakata, S. Kitagawa, *Science* **2013**, *339*, 193.
[25] S. A. Moggach, T. D. Bennett, A. K. Cheetham, *Angew. Chem., Int. Ed.* **2009**, *121*, 7221.
[26] C. Serre, F. Millange, C. Thouvenot, M. Noguès, G. Marsolier, D. Louër, G. Férey, *J. Am. Chem. Soc.* **2002**, *124*, 13519.
[27] N. C. Burtch, A. Torres-Knoop, G. S. Foo, J. Leisen, C. Sievers, B. Ensing, D. Dubbeldam, K. S. Walton, *J. Phys. Chem. Lett.* **2015**, *6*, 812.
[28] T. D. Bennett, A. K. Cheetham, A. H. Fuchs, F.-X. Coudert, *Nat. Chem.* **2017**, *9*, 11.
[29] S. Krause, V. Bon, I. Senkovska, U. Stoeck, D. Wallacher, D. M. Többens, S. Zander, R. S. Pillai, G. Maurin, F. Coudert, S. Kaskel, *Nature* **2016**, *532*, 348.
[30] D. Dubbeldam, K. S. Walton, D. E. Ellis, R. Q. Snurr, *Angew. Chem.* **2007**, *46*, 4496.
[31] Z. Fang, B. Bueken, D. E. De Vos, R. A. Fischer, *Angew. Chem., Int. Ed.* **2015**, *54*, 7234.
[32] H. L. Jiang, T. A. Makal, H. C. Zhou, *Coord. Chem. Rev.* **2013**, *257*, 2232.
[33] G. Wu, J. Huang, Y. Zang, J. He, G. Xu, *J. Am. Chem. Soc.* **2016**, *139*, 1360.
[34] J. D. Ferry, *Viscoelastic Properties of Polymers*, John Wiley & Sons, New York **1980**.
[35] A. K. Chaudhari, I. Han, J. C. Tan, *Adv. Mater.* **2015**, *27*, 4438.
[36] R. Hill, *Proc. Phys. Soc. Sect. A* **1952**, *65*, 349.
[37] S. I. Ranganathan, M. Ostoja-Starzewski, *Phys. Rev. Lett.* **2008**, *101*, 55504.
[38] S. F. Pugh, *London, Edinburgh, Dublin Philos. Mag. J. Sci.* **1954**, *45*, 823.
[39] H. Niu, X. Chen, P. Liu, W. Xing, X. Cheng, D. Li, Y. Li, *Sci. Rep.* **2012**, *2*, 718.
[40] G. J. Snyder, E. S. Toberer, *Nat. Mater.* **2008**, *7*, 105.
[41] D. R. Clarke, *Surf. Coat. Technol.* **2003**, *163*, 67.
[42] J. Feng, B. Xiao, J. Chen, Y. Du, J. Yu, R. Zhou, *Mater. Des.* **2011**, *32*, 3231.
[43] R. W. Munn, *J. Phys. C: Solid State Phys.* **1972**, *5*, 535.
[44] T. I. Zohdi, P. Wriggers, *Int. J. Numer. Methods Eng.* **2001**, *50*, 2573.
[45] J. C. Tan, B. Civalleri, C. C. Lin, L. Valenzano, R. Galvelis, P. F. Chen, T. D. Bennett, C. Mellot-Draznieks, C. M. Zicovich-Wilson, A. K. Cheetham, *Phys. Rev. Lett.* **2012**, *108*, 95502.
[46] A. Jayaraman, *Rev. Mod. Phys.* **1983**, *55*, 65.
[47] D. Tranchida, Z. Kiflie, S. Piccarolo, *Mod. Res. Educ.* **2007**, *20*, 737.
[48] L. Calabri, N. Pugno, C. Menozzi, S. Valeri, *J. Phys. Condens. Matter* **2008**, *20*, 474208.
[49] P. G. Yot, K. Yang, F. Ragon, V. Dmitriev, T. Devic, P. Horcajada, C. Serre, G. Maurin, *Dalton Trans.* **2016**, *45*, 4283.
[50] R. Vacher, L. Boyer, *Phys. Rev. B* **1972**, *6*, 639.
[51] K. Chapman, G. Halder, P. Chupas, *J. Am. Chem. Soc* **2009**, *131*, 17546.
[52] X. Du, J. Zhao, *npj Comput. Mater.* **2017**, *3*, 17.
[53] Y. Sun, Z. Hu, D. Zhao, K. Zeng, *ACS Appl. Mater. Interfaces* **2017**, *9*, 32202.
[54] J. C. Tan, T. D. Bennett, A. K. Cheetham, *Proc. Natl. Acad. Sci. USA* **2010**, *107*, 9938.
[55] S. Henke, W. Li, A. K. Cheetham, *Chem. Sci.* **2014**, *5*, 2392.
[56] T. D. Bennett, P. Simoncic, S. A. Moggach, F. Gozzo, P. Macchi, D. A. Keen, J. Tan, A. K. Cheetham, *Chem. Commun.* **2011**, *47*, 7983.
[57] K. Yang, G. Zhou, Q. Xu, *RSC Adv.* **2016**, *6*, 37506.
[58] G. D. Gatta, Y. Lee, *Mineral. Mag.* **2014**, *78*, 267.
[59] B. Van de Voorde, R. Ameloot, I. Stassen, M. Everaert, D. De Vos, J. Tan, *J. Mater. Chem. C* **2013**, *1*, 7716.
[60] J. Lewis, *Mater. Today* **2006**, *9*, 38.
[61] L. Pan, Z. Ji, X. Yi, X. Zhu, X. Chen, J. Shang, G. Liu, R.-W. Li, *Adv. Funct. Mater.* **2015**, *25*, 2677.
[62] Y. Liu, H. Wang, W. Shi, W. Zhang, J. Yu, B. K. Chandran, C. Cui, B. Zhu, Z. Liu, D. Bin Li, C. Xu, Z. Xu, P. S. Li, W. Huang, F. Huo, X. Chen, *Angew. Chem., Int. Ed.* **2016**, *128*, 9030.
[63] Q. Yang, D. Liu, C. Zhong, J.-R. Li, *Chem. Rev.* **2013**, *113*, 8261.
[64] J. D. Evans, G. Fraux, R. Gaillac, D. Kohen, F. Trousselet, J.-M. Vanson, F.-X. Coudert, *Chem. Mater.* **2017**, *29*, 199.
[65] K. Banlusan, E. Antillon, A. Strachan, *J. Phys. Chem. C* **2015**, *119*, 25845.
[66] E. T. Lilleodden, J. A. Zimmerman, S. M. Foiles, W. D. Nix, *J. Mech. Phys. Solids* **2003**, *51*, 901.
[67] L. E. Shilkrot, R. E. Miller, W. A. Curtin, *Phys. Rev. Lett.* **2002**, *89*, 25501.
[68] E. B. Tadmor, R. Phillips, M. Ortiz, *Langmuir* **1996**, *12*, 4529.
[69] J. D. Clayton, *Philos. Mag.* **2012**, *92*, 2860.
[70] H. T. Banks, S. Hu, Z. R. Kenz, *Adv. Appl. Math. Mech.* **2011**, *3*, 1.
[71] J. H. Irving, J. G. Kirkwood, *J. Chem. Phys.* **1950**, *18*, 817.
[72] E. Smith, *PhD Thesis*, Imperial College, London **2013**.
[73] D. Davydov, P. Steinmann, *Math. Mech. Solids* **2014**, *19*, 852.
[74] D. Davydov, P. Steinmann, *Math. Mech. Solids* **2015**, *20*, 1153.
[75] D. Davydov, P. Steinmann, *Math. Mech. Solids* **2013**, *19*, 411.
[76] F. D. Murnaghan, *Finite Deformation of an Elastic Solid*, Wiley, New York **1951**.

[77] J. A. Zimmerman, R. E. Jones, J. A. Templeton, *J. Comput. Phys.* **2010**, *229*, 2364.
[78] L. Kantorovich, *Quantum Theory of the Solid State: An Introduction*, Kluwer Academic Publishers, Dordrecht, The Netherlands **2004**.
[79] M. Born, K. Huang, *Dynamical Theory of Crystal Lattices*, Clarendon Press, Oxford **1957**.
[80] R. Hill, F. Milstein, *Phys. Rev. B* **1977**, *15*, 3087.
[81] D. C. Wallace, *Thermodynamics of Crystals*, John Wiley, New York **1972**.
[82] P. Marcus, H. Ma, S. Qiu, *J. Phys. Condens. Matter* **2002**, *14*, 525.
[83] G. Steinle-Neumann, R. E. Cohen, *J. Phys. Condens. Matter* **2004**, *16*, 8783.
[84] P. Marcus, S. L. Qiu, *J. Phys. Condens. Matter* **2004**, *16*, 8787.
[85] P. M. Marcus, S. L. Qiu, *J. Phys. Condens. Matter* **2009**, *21*, 115401.
[86] A. R. Oganov, in *Treatise on Geophyics*, Elsevier, Amsterdam **2007**, pp. 195–210.
[87] J. R. Ray, A. Rahman, *J. Chem. Phys.* **1984**, *80*, 4423.
[88] J. R. Ray, A. Rahman, *J. Chem. Phys.* **1985**, *82*, 4243.
[89] Z. Zhou, B. Joós, *Phys. Rev. B* **1996**, *54*, 3841.
[90] Z. Zhou, B. Joos, *Phys. Rev. B* **2002**, *66*, 541011.
[91] Z. Zhou, *Chinese J. Phys.* **2004**, *42*, 21.
[92] G. Kresse, J. Hafner, *Phys. Rev. B* **1993**, *47*, 558.
[93] G. Kresse, J. Furthmüller, *Phys. Rev. B* **1996**, *54*, 11169.
[94] R. Dovesi, R. Orlando, A. Erba, C. M. Zicovich-wilson, B. Civalleri, S. Casassa, L. Maschio, M. Ferrabone, M. D. La Pierre, P. D. Arco, Y. No, M. Caus, *Quantum Chem.* **2014**, *114*, 1287.
[95] D. E. P. Vanpoucke, K. Lejaeghere, V. Van Speybroeck, M. Waroquier, A. Ghysels, *J. Phys. Chem. C* **2015**, *119*, 23752.
[96] A. U. Ortiz, A. Boutin, A. H. Fuchs, F.-X. Coudert, *J. Chem. Phys.* **2013**, *138*, 174703.
[97] A. U. Ortiz, A. Boutin, A. H. Fuchs, F.-X. Coudert, *Phys. Rev. Lett.* **2012**, *109*, 195502.
[98] M. R. Ryder, B. Civalleri, J.-C. Tan, *Phys. Chem. Chem. Phys.* **2016**, *18*, 9079.
[99] J. F. Lutsko, *J. Appl. Phys.* **1989**, *65*, 2991.
[100] J. D. Gale, *JCS Faraday Trans.* **1997**, *93*, 629.
[101] D. Dubbeldam, S. Calero, D. E. Ellis, R. Q. Snurr, *Mol. Simul.* **2016**, *42*, 81.
[102] D. Dubbeldam, R. Krishna, *J. Phys. Chem. C* **2009**, *113*, 19317.
[103] J. Heinen, N. C. Burtch, K. S. Walton, D. Dubbeldam, *J. Chem. Theory Comput.* **2017**, *13*, 3722.
[104] M. Parrinello, *J. Chem. Phys.* **2008**, *76*, 2662.
[105] J. R. Ray, *Comput. Phys. Rep.* **1988**, *8*, 111.
[106] K. Workum, J. Pablo, *Phys. Rev. E* **2003**, *67*, 2.
[107] P. J. Fay, J. R. Ray, *Phys. Rev. A* **1992**, *46*, 4645.
[108] G. Clavier, N. Desbiens, E. Bourasseau, V. Lachet, N. Brusselle-Dupenda, B. Rousseau, *Mol. Simul.* **2017**, *43*, 1413.
[109] T. H. K. Barron, M. L. Klein, *Proc. Phys. Soc.* **1965**, *85*, 523.
[110] H. Gao, W. Wei, L. Dong, G. Feng, X. Jiang, R. Wu, Z. Lin, W. Li, *Crystals* **2017**, *7*, 99.
[111] H. Wu, T. Yildirim, W. Zhou, *J. Phys. Chem. Lett.* **2013**, *4*, 925.
[112] C. L. Hobday, R. J. Marshall, C. F. Murphie, J. Sotelo, T. Richards, D. R. Allan, T. Düren, F. X. Coudert, R. S. Forgan, C. A. Morrison, S. A. Moggach, T. D. Bennett, *Angew. Chem., Int. Ed.* **2016**, *55*, 2401.
[113] M. R. Ryder, B. Civalleri, T. Bennett, S. Henke, S. Rudić, G. Cinque, F. Fernandez-Alonso, J. C. Tan, *Phys. Rev. Lett.* **2014**, *113*, 1.
[114] M. R. Ryder, B. Van De Voorde, B. Civalleri, T. D. Bennett, S. Mukhopadhyay, G. Cinque, F. Fernandez-Alonso, D. De Vos, S. Rudić, J. C. Tan, *Phys. Rev. Lett.* **2017**, *118*, 255502.
[115] O. V. Gutov, M. G. Hevia, E. C. Escudero-Adán, A. Shafir, *Inorg. Chem.* **2015**, *54*, 8396.
[116] D. S. Sholl, R. P. Lively, *J. Phys. Chem. Lett.* **2015**, *6*, 3437.
[117] M. J. Cliffe, W. Wan, X. Zou, P. A. Chater, A. K. Kleppe, M. G. Tucker, H. Wilhelm, N. P. Funnell, F.-X. Coudert, A. L. Goodwin, *Nat. Commun.* **2014**, *5*, 1.
[118] M. Vandichel, J. Hajek, A. Ghysels, A. De Vos, M. Waroquier, V. Van Speybroeck, *CrystEngComm* **2016**, *18*, 7056.
[119] A. W. Thornton, R. Babarao, A. Jain, F. Trousselet, F. X. Coudert, *Daltan Trans.* **2016**, *45*, 4352.
[120] S. J. Lee, C. Doussot, A. Baux, L. Liu, G. B. Jameson, C. Richardson, J. J. Pak, F. Trousselet, F. X. Coudert, S. G. Telfer, *Chem. Mater.* **2016**, *28*, 368.
[121] T. D. Bennett, A. K. Cheetham, *Acc. Chem. Res.* **2014**, *47*, 1555.
[122] A. U. Ortiz, A. Boutin, A. H. Fuchs, F. X. Coudert, *J. Phys. Chem. Lett.* **2013**, *4*, 1861.
[123] S. M. J. Rogge, J. Wieme, L. Vanduyfhuys, S. Vandenbrande, G. Maurin, T. Verstraelen, M. Waroquier, V. Van Speybroeck, *Chem. Mater.* **2016**, *28*, 5721.
[124] T. D. Bennett, T. K. Todorova, E. F. Baxter, D. G. Reid, C. Gervais, B. Bueken, B. Van de Voorde, D. De Vos, D. A. Keen, C. Mellot-Draznieks, *Phys. Chem. Chem. Phys.* **2016**, *18*, 2192.
[125] S. Sachdeva, A. Pustovarenko, E. J. R. Sudhölter, F. Kapteijn, L. C. P. M. de Smet, J. Gascon, *CrystEngComm* **2016**, *18*, 4018.
[126] S. Yang, X. Lin, W. Lewis, M. Suyetin, E. Bichoutskaia, J. E. Parker, C. C. Tang, D. R. Allan, P. J. Rizkallah, P. Hubberstey, N. R. Champness, K. Mark Thomas, A. J. Blake, M. Schröder, *Nat. Mater.* **2012**, *11*, 710.
[127] E. Proietti, F. Jaouen, M. Lefèvre, N. Larouche, J. Tian, J. Herranz, J.-P. Dodelet, *Nat. Commun.* **2011**, *2*, 416.
[128] M. Klimakow, P. Klobes, A. F. Thünemann, K. Rademann, F. Emmerling, *Chem. Mater.* **2010**, *22*, 5216.
[129] H. Qi, S. S. Iyengar, K. Chakrabarty, *J. Franklin Inst.* **2001**, *338*, 655.
[130] P. Kumar, L. Morawska, C. Martani, G. Biskos, M. Neophytou, S. Di Sabatino, M. Bell, L. Norford, R. Britter, *Environ. Int.* **2015**, *75*, 199.
[131] X. Li, D.-W. Lee, *Meas. Sci. Technol.* **2012**, *23*, 29501.
[132] M. Madou, *From MEMS to Bio-MEMS and Bio-NEMS: Manufacturing Techniques and Applications*, CRC Press, Taylor & Francis Group, Boca Raton, FL **2011**.
[133] D. S. Ballantine Jr., R. M. White, S. J. Martin, A. J. Ricco, E. T. Zellers, G. C. Frye, H. Wohltjen, *Acoustic Wave Sensors: Theory, Design and Physico-Chemical Applications*, Academic Press, Chestnut Hill, MA **1997**.
[134] M. D. Allendorf, R. J. T. Houk, L. Andruszkiewicz, A. A. Talin, J. Pikarsky, A. Choudhury, K. A. Gall, P. J. Hesketh, *J. Am. Chem. Soc.* **2008**, *130*, 14404.
[135] I. Ellern, A. Venkatasubramanian, J. H. Lee, P. J. Hesketh, V. Stavila, M. D. Allendorf, A. L. Robinson, *ECS Trans.* **2012**, *50*, 469.
[136] J.-H. Lee, R. T. J. Houk, A. Robinson, J. A. Greathouse, S. M. Thornberg, M. D. Allendorf, P. J. Hesketh, in *Proc. SPIE Defense, Security, and Sensing*, Orlando, FL USA, **2010**, p. 767927/1.
[137] C. Yim, M. Lee, W. Kim, S. Lee, G.-H. Kim, K. T. Kim, S. Jeon, *Chem. Commun.* **2015**, *51*, 6168.
[138] C. Yim, M. Lee, M. Yun, G.-H. Kim, K. T. Kim, S. Jeon, *Sci. Rep.* **2015**, *5*, 10674.
[139] A. Venkatasubramanian, J. Lee, V. Stavila, A. Robinson, M. D. Allendorf, P. J. Hesketh, *Sens. Actuators, B* **2012**, *168*, 256.
[140] A. Schoedel, Z. Ji, O. M. Yaghi, *Nat. Energy* **2016**, *1*, 16034.
[141] J. A. Mason, J. Oktawiec, M. K. Taylor, M. R. Hudson, J. Rodriguez, J. E. Bachman, M. I. Gonzalez, A. Cervellino, A. Guagliardi, C. M. Brown, P. L. Llewellyn, N. Masciocchi, J. R. Long, *Nature* **2015**, *527*, 357.
[142] R. Q. Snurr, B. Smit, Y. G. Chung, R. L. Martin, R. Mercado, M. W. Deem, *Energy Environ. Sci.* **2015**, *8*, 1190.
[143] *Industrial Technologies Program Materials*, Oak Ridge National Laboratory **2005**. https://www1.eere.energy.gov/manufacturing/industries_technologies/imf/pdfs/separationsreport.pdf (accessed: November 2017).
[144] J. L. Humphrey, G. E. Keller, *Separation Process Technology*, McGraw-Hill, New York **1997**.

[145] D. M. Ruthven, *Principles of Adsorption and Adsorption Processes*, John Wiley & Sons, New York **1984**.
[146] H. Sato, W. Kosaka, R. Matsuda, A. Hori, Y. Hijikata, R. V. Belosludov, S. Sakaki, M. Takata, S. Kitagawa, *Science* **2014**, *343*, 167.
[147] T. M. Mcdonald, J. A. Mason, X. Kong, E. D. Bloch, D. Gygi, A. Dani, V. Crocella, F. Giordanino, S. O. Odoh, W. S. Drisdell, B. Vlaisavljevich, A. L. Dzubak, R. Poloni, S. K. Schnell, N. Planas, K. Lee, T. Pascal, L. F. Wan, D. Prendergast, J. B. Neaton, *Nature* **2015**, *519*, 303.
[148] L. Sun, M. G. Campbell, M. Dinca, *Angew. Chem., Int. Ed.* **2016**, *55*, 3566.
[149] A. A. Talin, A. Centrone, A. C. Ford, M. E. Foster, V. Stavila, P. Haney, R. A. Kinney, V. Szalai, F. El Gabaly, H. P. Yoon, F. Léonard, M. D. Allendorf, *Science* **2013**, *343*, 66.
[150] H. Ghermezcheshme, M. Mohseni, H. Yahyaei, *Tribol. Int.* **2015**, *88*, 66.
[151] M. Wong, G. Lim, A. Moyse, J. Reddy, H.-J. Sue, *Wear* **2004**, *256*, 1214.
[152] W. J. Koros, C. Zhang, *Nat. Mater.* **2017**, *52*, 4363.
[153] J. A. Thornton, D. W. Hoffman, *Thin Solid Films* **1989**, *171*, 5.
[154] C. A. Swenson, *J. Phys. Chem. Ref. Data* **1983**, *12*, 179.
[155] R. Buffington, W. Latimer, *J. Am. Chem. Soc.* **1926**, *48*, 2305.
[156] W. Zhou, H. Wu, T. Yildirim, J. R. Simpson, A. R. H. Walker, *Phys. Rev. B* **2008**, *78*, 54114.
[157] N. C. Burtch, D. Dubbeldam, K. S. Walton, *Mol. Simul.* **2015**, *41*, 1379.
[158] J. A. Greathouse, M. D. Allendorf, *J. Phys. Chem. C* **2008**, *112*, 5795.
[159] Y. Wu, A. Kobayashi, G. Halder, V. Peterson, K. Chapman, N. Lock, P. Southon, C. Kepert, *Angew. Chem.* **2008**, *120*, 9061.
[160] F. Shen, P. Lu, S. J. O'Shea, K. H. Lee, T. Y. Ng, *Sens. Actuators, A* **2001**, *95*, 17.
[161] N. C. Burtch, K. S. Walton, *Acc. Chem. Res.* **2015**, *48*, 2850.
[162] H. Jasuja, N. C. Burtch, Y. Huang, Y. Cai, K. S. Walton, *Langmuir* **2013**, *29*, 633.
[163] C. Yang, U. Kaipa, Q. Z. Mather, X. Wang, V. Nesterov, A. F. Venero, M. A. Omary, *J. Am. Chem. Soc.* **2011**, *133*, 18094.
[164] J. B. Decoste, G. W. Peterson, M. W. Smith, C. A. Stone, C. R. Willis, *J. Am. Chem. Soc.* **2012**, *134*, 1486.
[165] H.-L. Jiang, D. Feng, K. Wang, Z.-Y. Gu, Z. Wei, Y.-P. Chen, H.-C. Zhou, *J. Am. Chem. Soc.* **2013**, *135*, 13934.
[166] V. Bon, V. Senkovskyy, I. Senkovska, S. Kaskel, *Chem. Commun.* **2012**, *48*, 8407.
[167] N. C. Burtch, H. Jasuja, K. S. Walton, *Chem. Rev.* **2014**, *114*, 10575.
[168] R. M. Heck, S. Gulati, R. J. Farrauto, *Chem. Eng. J.* **2001**, *82*, 149.
[169] L. A. Darunte, Y. Terada, C. R. Murdock, K. S. Walton, D. S. Sholl, C. W. Jones, *ACS Appl. Mater. Interfaces* **2017**, *9*, 17042.
[170] P. Kusgens, A. Zgaverdea, H. Fritz, S. Siegle, S. Kaskel, *J. Am. Ceram. Soc.* **2010**, *93*, 2476.
[171] W. J. Koros, C. Zhang, *Nat. Mater.* **2017**, *16*, 289.
[172] J. D. Evans, F.-X. Coudert, *J. Phys. Chem. Lett.* **2017**, *8*, 1578.
[173] Y. Peng, V. Krungleviciute, I. Eryazici, J. T. Hupp, O. K. Farha, T. Yildirim, *J. Am. Chem. Soc.* **2013**, *135*, 11887.
[174] J. J. Purewal, D. Liu, J. Yang, A. Sudik, D. J. Siegel, S. Maurer, U. Muller, *Int. J. Hydrogen Energy* **2012**, *37*, 2723.
[175] N. Chanut, A. D. Wiersum, U. H. Lee, Y. K. Hwang, F. Ragon, H. Chevreau, S. Bourrelly, B. Kuchta, J. S. Chang, C. Serre, P. L. Llewellyn, *Eur. J. Inorg. Chem.* **2016**, *2016*, 4416.
[176] H. J. Choi, M. Dinca, J. R. Long, *J. Am. Chem. Soc.* **2008**, *130*, 7848.
[177] A. A. Talin, R. E. Jones, P. E. Hopkins, *MRS Bull.* **2016**, *41*, 877.
[178] M. D. Allendorf, M. E. Foster, V. Stavila, P. L. Feng, F. P. Doty, K. Leong, E. Y. Ma, S. R. Johnston, A. A. Talin, *J. Phys. Chem. Lett.* **2015**, *6*, 1182.
[179] Y.-P. Chen, Y. Liu, D. Liu, M. Bosch, H.-C. Zhou, *J. Am. Chem. Soc.* **2015**, *137*, 2919.
[180] P. G. Yot, Z. Boudene, J. Macia, D. Granier, L. Vanduyfhuys, T. Verstraelen, V. Van Speybroeck, T. Devic, C. Serre, G. Férey, N. Stock, G. Maurin, *Chem. Commun.* **2014**, *50*, 9462.
[181] J. Rodriguez, I. Beurroies, T. Loiseau, R. Denoyel, P. L. Llewellyn, *Angew. Chem., Int. Ed.* **2015**, *54*, 4626.
[182] Y. Miao, Z. Su, K. S. Suslick, *J. Am. Chem. Soc.* **2017**, *139*, 4667.
[183] Y. G. Chung, J. Camp, M. Haranczyk, B. J. Sikora, W. Bury, V. Krungleviciute, T. Yildirim, O. K. Farha, D. S. Sholl, R. Q. Snurr, *Chem. Mater.* **2014**, *26*, 6185.
[184] D. Nazarian, J. S. Camp, Y. G. Chung, R. Q. Snurr, D. S. Sholl, *Chem. Mater.* **2016**, *29*, 2521.
[185] T. D. Bennett, J. Tan, Y. Yue, E. Baxter, C. Ducati, N. J. Terrill, H. H. Yeung, Z. Zhou, W. Chen, S. Henke, A. K. Cheetham, G. N. Greaves, *Nat. Commun.* **2015**, *6*, 8079.
[186] D. Umeyama, S. Horike, M. Inukai, T. Itakura, S. Kitagawa, *J. Am. Chem. Soc.* **2015**, *137*, 864.
[187] R. Gaillac, P. Pullumbi, K. A. Beyer, K. W. Chapman, D. A. Keen, T. D. Bennett, F. Coudert, unpublished.
[188] K. W. Chapman, D. F. Sava, G. J. Halder, P. J. Chupas, T. M. Nenoff, *J. Am. Chem. Soc.* **2011**, *133*, 18583.
[189] T. D. Bennett, P. J. Saines, D. A. Keen, J. Tan, A. K. Cheetham, **2013**, *7541*, 1.
[190] S. Sakaida, K. Otsubo, O. Sakata, C. Song, A. Fujiwara, M. Takata, H. Kitagawa, *Nat. Chem.* **2016**, *8*, 377.
[191] N. Kavoosi, V. Bon, I. Senkovska, S. Krause, C. Atzori, F. Bonino, J. Pallmann, S. Paasch, E. Brunnerc, S. Kaskel, *Dalton Trans.* **2017**, *46*, 4685.

